

Rapid formation of large dust grains in the luminous supernova SN 2010jl

Christa Gall^{1,2,3}, Jens Hjorth², Darach Watson², Eli Dwek³, Justyn R. Maund^{4,2}, Ori Fox⁵, Giorgos Leloudas^{6,2}, Daniele Malesani² & Avril C. Day-Jones⁷

¹*Department of Physics and Astronomy, Aarhus University, Ny Munkegade 120, DK-8000 Aarhus C, Denmark*

²*Dark Cosmology Centre, Niels Bohr Institute, University of Copenhagen, Juliane Maries Vej 30, DK-2100 Copenhagen Ø, Denmark*

³*Observational Cosmology Lab, Code 665, NASA Goddard Space Flight Center, Greenbelt, MD 20771, USA*

⁴*Astrophysics Research Centre School of Mathematics and Physics Queen's University Belfast Belfast BT7 1NN, UK*

⁵*Department of Astronomy, University of California, Berkeley, CA 94720-3411, USA*

⁶*The Oskar Klein Centre, Department of Physics, Stockholm University, Albanova University Centre, 10691, Stockholm, Sweden*

⁷*Departamento de Astronomia, Universidad de Chile, Camino del Observatorio 1515, Santiago, Chile*

The origin of dust in galaxies is still a mystery (1, 2, 3, 4). The majority of the refractory elements are produced in supernova explosions but it is unclear how and where dust grains condense and grow, and how they avoid destruction in the harsh environments of star-forming

galaxies. The recent detection of 0.1–0.5 solar masses of dust in nearby supernova remnants (5, 6, 7) suggests *in situ* dust formation, while other observations reveal very little dust in supernovae the first few years after explosion (1, 8, 9, 10). Observations of the bright SN 2010jl have been interpreted as pre-existing dust (11), dust formation (12, 13) or no dust at all (14). Here we report the rapid (40–240 days) formation of dust in its dense circumstellar medium. The wavelength dependent extinction of this dust reveals the presence of very large ($> 1 \mu\text{m}$) grains, which are resistant to destructive processes (15). At later times (500–900 days), the near-IR thermal emission shows an accelerated growth in dust mass, marking the transition of the supernova from a circumstellar- to an ejecta-dominated source of dust. This provides the link between the early and late dust mass evolution in supernovae with dense circumstellar media.

We observed the bright ($V \sim 14$) and luminous ($M_V \sim -20$) Type IIn SN 2010jl (16) with the VLT/X-shooter spectrograph covering the wide wavelength range 0.3–2.5 μm . Peak brightness occurred on 2010 Oct 18.6 UT, and observations were made at 9 early epochs and at one late epoch, 26–239 and 868 days past peak, respectively (Methods, Extended Data Table 1, Extended Data Figures 1–5). Figure 1 shows the intermediate-width components of the hydrogen emission lines of H γ at $\lambda 4340.472$ and P β at $\lambda 12818.072$ and of the oxygen ejecta emission lines [O I] $\lambda 16300.304$, 6363.776 (rest frame). The emission profiles change with time, exhibiting a substantial depression of the red wings and a corresponding blueshift of the centroids of the lines (Extended Data Figure 6) due to preferential extinction of the emission from the receding material on the far side of the supernova (12, 17, 18). The effect is less pronounced at longer wavelengths, as expected

if the attenuation of the lines is due to dust extinction, and rules out that the blueshifts are due to electron scattering (14) (Supplementary Information). The early epoch hydrogen lines have a Lorentzian half width at half maximum (HWHM) in the range 1,000–2,000 km s⁻¹. The middle and right panels of Figure 1 show that the line profiles at the late epoch are narrower (HWHM $\sim 800 \pm 100$ km s⁻¹) and also exhibit blueshifts of the oxygen lines, which indicates that ejecta material is involved in the dust formation at this stage.

Figure 2 shows the temporal evolution of the inferred extinction, A_λ , as derived from the attenuation of emission lines in the early spectra. The extinction has been calculated from the ratios of the integrated line profiles at each epoch. We assume that the first epoch at 26 days past peak is nearly unextinguished and use it as a reference. The monotonic increase of the extinction as a function of time indicates continuous formation of dust. The extinction at 239 days is $A_V \sim 0.6$ mag. Interestingly, the shape of the normalized extinction curve shows no substantial variation with time. Scaling and combining the data from the eight individual early epochs allows us to produce the first directly measured, robust extinction curve for a supernova. The extinction curve is shallow, with $R_V = A_V/E(B - V) \approx 6.4$, and can be represented by a mix of grey-extinction dust grains ($A_\lambda = \text{constant}$) and either standard Small Magellanic Cloud (SMC) or Milky Way (MW) extinction grains (19). The extinction contribution of the grey dust is 40 % in the V band. We fit several dust models to the extinction curve using amorphous carbon dust characterized by a power-law grain size distribution (20) with slope α , and minimum and maximum grain radii ($a_{\min} < a_{\max}$) in the interval [0.001, 5.0] μm .

Figure 3 shows the resulting confidence interval for the two parameters a_{\max} and α around the best fit values of $a_{\min} = 0.001 \mu\text{m}$, $a_{\max} = 4.2 \mu\text{m}$ and $\alpha = 3.6$. It is evident that only size distributions extending to grain radii that are significantly larger than that of MW interstellar medium (21, 22) dust ($\geq 0.25 \mu\text{m}$) can reproduce the supernova extinction curve (Figure 2). The 2σ lower limit on the maximum grain size is $a_{\max} > 0.7 \mu\text{m}$. We cannot perform a similar analysis of the late epoch because the intrinsic line profile at this epoch is unknown and likely highly affected by extinction (13). However, we note that the blueshift velocities change only marginally with wavelength (Extended Data Figure 6), suggestive of large grains also at this epoch.

Figure 4 illustrates the continuous build-up of dust as a function of time. The increasing attenuation of the lines is accompanied by increasing emission in the near-infrared (NIR) spectra, from a slight excess over a supernova blackbody fit at early times to total dominance at the late epoch. We fitted the spectra with black bodies which for the NIR excess yield a constant black-body radius of $(1.0 \pm 0.2) \times 10^{16}$ cm at the early epochs, and a temperature that declines from $\sim 2,300$ K to $\sim 1,600$ K from day 26 onwards. At the late epoch, we obtain a black-body radius of $(5.7 \pm 0.2) \times 10^{16}$ cm and a temperature of $\sim 1,100$ K. The high temperatures detected at the early epochs suggest that the NIR excess is due to thermal emission from carbonaceous dust, rather than silicate dust, which has a lower condensation temperature of $\sim 1,500$ K (1). The high temperatures rule out suggestions that the NIR emission is due to pre-existing dust or a dust echo (11) (Extended Data Figures 7, 8, Supplementary Information). Fitting the NIR excess with a modified black body, assuming the grain composition found in our analysis of the extinction curve (Figure 3), gives a dust temperature similar to the black-body temperature, which is at all epochs (and considered dust

compositions) larger than 1,000 K. The dust masses inferred from the extinction and NIR emission agree very well. The inferred amount of dust at the late epoch (868 days) is $\sim 2.5 \times 10^{-3} M_{\odot}$ if composed of carbon, but could be up to an order of magnitude larger for silicates (Methods). Our results indicate accelerated dust formation after several hundred days. SN 2010jl will contain a dust mass of $\sim 0.5 M_{\odot}$ similar to that observed in SN 1987A (5, 6), by day ~ 8000 , if the dust production continues to follow the trend depicted in Figure 4.

The most obvious location for early dust formation is in a cool, dense shell behind the supernova shock (18, 23), which sweeps up material as it propagates through the dense circumstellar shell surrounding SN 2010jl (24) (Supplementary Information). Dust formation in the ejecta is impossible at this stage because the temperature is too high. The postshock gas cools and gets compressed to the low temperatures and high densities necessary for dust formation and gives rise to the observed intermediate width emission lines. By the time of our first observation 26 days past peak, the supernova blast wave encounters the dense circumstellar shell at a radius of $\sim 2.0 \times 10^{16}$ cm for a blast wave velocity of $\sim 3.5 \times 10^4$ km s $^{-1}$. As indicated by the blueshifts of the ejecta metal lines (Figure 1), the accelerated dust formation occurring at later times (Figure 4) and at larger radius is possibly facilitated by the bulk ejecta material, which travels on average at a velocity of $\sim 7,500$ km s $^{-1}$ at early epochs (Extended Data Figure 4).

Our detection of large grains soon after the supernova explosion suggests a remarkably rapid and efficient mechanism for dust nucleation and growth. The underlying physics is poorly understood but may involve a two-stage process governed by early dust formation in a cool, dense shell,

followed by accelerated dust formation involving ejecta material. For Type IIP supernovae, the growth of dust grains can be sustained up to 5 years past explosion (25). The dense CSM around Type IIn supernovae may provide conditions to facilitate dust growth beyond that. The process appears generic, in that other Type IIn supernovae like SN 1995N, SN 1998S, SN 2005ip, and SN 2006jd exhibited similar observed NIR properties (8, 10, 26, 27) and growing dust masses, consistent with the trend revealed here for SN 2010jl (Figure 4). Moreover, it establishes a link between the early small dust masses inferred in supernovae (1, 8, 10) and the large dust masses found in a few supernova remnants (1, 5, 7). Large grains ($0.1 \leq a_{\max} \lesssim 4.0 \mu\text{m}$), provide an effective way to counter destructive processes in the interstellar medium (28). Indeed, large grains from the interstellar medium have been detected in the Solar System (29). Simulations indicate that grains larger than $\sim 0.1 \mu\text{m}$ will survive reverse shock interactions with only a low fraction being sputtered to smaller radii (15). For a grain size distribution of $a_{\min} = 0.001 \mu\text{m}$, $a_{\max} = 4.2 \mu\text{m}$ and $\alpha = 3.6$ (Figures 2 and 3), the mass fraction of grains above $0.1 \mu\text{m}$ is $\sim 80 \%$, i.e., the majority of the produced dust mass can be retained.

Methods summary

We obtained optical and near-infrared medium-resolution spectroscopy with the ESO VLT/X-shooter instrument of the bright Type II_n supernova SN 2010jl at 9 epochs between 2010 November 13.4 UT and 2011 June 15.0 UT. The continuum emission of the spectra was fit with a combination of black-body, modified black-body and host galaxy models, allowing us to quantify the temporal progression of the temperature and radius of the photosphere as well as the temperature and characteristics of the forming dust, which causes conspicuous excess near-infrared emission. We analysed the profiles of the most prominent hydrogen, helium and oxygen emission lines. From Lorentzian profile fits, which are good representations of the emission lines, we measured the blueshifts of the peaks and the half widths at half maximum of the lines, and derived the wavelength dependent attenuation properties of the forming dust at each epoch. The uncertainties were obtained using Monte Carlo calculations by varying the Lorentzian profile parameters. We generated synthetic UBVRIJHK lightcurves and calculated the energy output of the supernova. This, together with calculated dust vaporization radii, temperatures of the dust grains at different distances from the supernova, and the radius evolution of the forward shock, were used to constrain the location of the forming dust. Different dust models, characterised by either single grain sizes or a power-law grain size distribution function and either amorphous carbon or silicates, were fitted to the extinction curves and the near-infrared excess emission. From these fits, we derived the temporal progression of the dust mass of the forming dust at each observed epoch.

- [1] Gall, C., Hjorth, J. & Andersen, A. C. Production of dust by massive stars at high redshift. *Astron. Astrophys. Rev.* **19**, 43 (2011). 1108.0403.
- [2] Matsuura, M. *et al.* The global gas and dust budget of the Large Magellanic Cloud: AGB stars and supernovae, and the impact on the ISM evolution. *Mon. Not. R. Astron. Soc.* **396**, 918–934 (2009). 0903.1123.
- [3] Draine, B. T. Interstellar Dust Models and Evolutionary Implications. In Henning, T., Grün, E. & Steinacker, J. (eds.) *Cosmic Dust - Near and Far*, vol. 414 of *Astronomical Society of the Pacific Conference Series*, 453 (2009). 0903.1658.
- [4] Dunne, L. *et al.* Herschel-ATLAS: rapid evolution of dust in galaxies over the last 5 billion years. *Mon. Not. R. Astron. Soc.* **417**, 1510–1533 (2011). 1012.5186.
- [5] Matsuura, M. *et al.* Herschel Detects a Massive Dust Reservoir in Supernova 1987A. *Science* **333**, 1258– (2011). 1107.1477.
- [6] Indebetouw, R. *et al.* Dust Production and Particle Acceleration in Supernova 1987A Revealed with ALMA. *Astrophys. J. Lett.* **782**, L2 (2014). 1312.4086.
- [7] Gomez, H. L. *et al.* A Cool Dust Factory in the Crab Nebula: A Herschel Study of the Filaments. *Astrophys. J.* **760**, 96 (2012). 1209.5677.
- [8] Pozzo, M. *et al.* On the source of the late-time infrared luminosity of SN 1998S and other Type II supernovae. *Mon. Not. R. Astron. Soc.* **352**, 457–477 (2004). astro-ph/0404533.

- [9] Otsuka, M. *et al.* Late-time Light Curves of Type II Supernovae: Physical Properties of Supernovae and Their Environment. *Astrophys. J.* **744**, 26 (2012). 1111.5041.
- [10] Stritzinger, M. *et al.* Multi-wavelength Observations of the Enduring Type II_n Supernovae 2005ip and 2006jd. *Astrophys. J.* **756**, 173 (2012). 1206.5575.
- [11] Andrews, J. E. *et al.* Evidence for Pre-existing Dust in the Bright Type II_n SN 2010jl. *Astron. J.* **142**, 45 (2011). 1106.0537.
- [12] Smith, N. *et al.* Systematic Blueshift of Line Profiles in the Type II_n Supernova 2010jl: Evidence for Post-shock Dust Formation? *Astron. J.* **143**, 17 (2012). 1108.2869.
- [13] Maeda, K. *et al.* Properties of Newly Formed Dust Grains in the Luminous Type II_n Supernova 2010jl. *Astrophys. J.* **776**, 5 (2013). 1308.0406.
- [14] Zhang, T. *et al.* Type II_n Supernova SN 2010jl: Optical Observations for over 500 Days after Explosion. *Astron. J.* **144**, 131 (2012). 1208.6078.
- [15] Silvia, D. W., Smith, B. D. & Shull, J. M. Numerical Simulations of Supernova Dust Destruction. I. Cloud-crushing and Post-processed Grain Sputtering. *Astrophys. J.* **715**, 1575–1590 (2010). 1001.4793.
- [16] Newton, J. & Puckett, T. Possible Supernova in UGC 5189A. *Central Bureau Electronic Telegrams* **2532**, 1 (2010).
- [17] Lucy, L. B., Danziger, I. J., Gouiffes, C. & Bouchet, P. Dust Condensation in the Ejecta of SN 1987 A. In Tenorio-Tagle, G., Moles, M. & Melnick, J. (eds.) *IAU Colloq. 120: Structure and*

Dynamics of the Interstellar Medium, vol. 350 of *Lecture Notes in Physics*, Berlin Springer Verlag, 164 (1989).

- [18] Smith, N., Foley, R. J. & Filippenko, A. V. Dust Formation and He II $\lambda 4686$ Emission in the Dense Shell of the Peculiar Type Ib Supernova 2006jc. *Astrophys. J.* **680**, 568–579 (2008). 0704.2249.
- [19] Gordon, K. D., Clayton, G. C., Misselt, K. A., Landolt, A. U. & Wolff, M. J. A Quantitative Comparison of the Small Magellanic Cloud, Large Magellanic Cloud, and Milky Way Ultraviolet to Near-Infrared Extinction Curves. *Astrophys. J.* **594**, 279–293 (2003). astro-ph/0305257.
- [20] Mathis, J. S., Rumpl, W. & Nordsieck, K. H. The size distribution of interstellar grains. *Astrophys. J.* **217**, 425–433 (1977).
- [21] Zubko, V., Dwek, E. & Arendt, R. G. Interstellar Dust Models Consistent with Extinction, Emission, and Abundance Constraints. *Astrophys. J. Suppl.* **152**, 211–249 (2004). astro-ph/0312641.
- [22] Brandt, T. D. & Draine, B. T. The Spectrum of the Diffuse Galactic Light: The Milky Way in Scattered Light. *Astrophys. J.* **744**, 129 (2012). 1109.4175.
- [23] Fox, O. *et al.* Near-Infrared Photometry of the Type II_n SN 2005ip: The Case for Dust Condensation. *Astrophys. J.* **691**, 650–660 (2009). 0807.3555.
- [24] Ofek, E. O. *et al.* SN 2010jl: Optical to Hard X-Ray Observations Reveal an Explosion Embedded in a Ten Solar Mass Cocoon. *Astrophys. J.* **781**, 42 (2014). 1307.2247.

- [25] Sarangi, A. & Cherchneff, I. The Chemically Controlled Synthesis of Dust in Type II-P Supernovae. *Astrophys. J.* **776**, 107 (2013). 1309.5887.
- [26] Mauerhan, J. & Smith, N. Supernova 1998S at 14 years postmortem: continuing circumstellar interaction and dust formation. *Mon. Not. R. Astron. Soc.* **424**, 2659–2666 (2012). 1204.1610.
- [27] Van Dyk, S. D. Late-time Dust Emission from the Type II_n Supernova 1995N. *Astron. J.* **145**, 118 (2013). 1305.0028.
- [28] Jones, A. P. & Nuth, J. A. Dust destruction in the ISM: a re-evaluation of dust lifetimes. *Astron. Astrophys.* **530**, A44 (2011).
- [29] Frisch, P. C. *et al.* Dust in the Local Interstellar Wind. *Astrophys. J.* **525**, 492–516 (1999). astro-ph/9905108.
- [30] Gallagher, J. S. *et al.* Optical and Infrared Analysis of Type II SN 2006bc. *Astrophys. J.* **753**, 109 (2012). 1205.5517.
- [31] Chandra, P. *et al.* Strong Evolution of X-Ray Absorption in the Type II_n Supernova SN 2010jl. *Astrophys. J. Lett.* **750**, L2 (2012). 1203.1614.
- [32] Ofek, E. O. *et al.* X-Ray Emission from Supernovae in Dense Circumstellar Matter Environments: A Search for Collisionless Shocks. *Astrophys. J.* **763**, 42 (2013). 1206.0748.

- [33] van Marle, A. J., Smith, N., Owocki, S. P. & van Veelen, B. Numerical models of collisions between core-collapse supernovae and circumstellar shells. *Mon. Not. R. Astron. Soc.* **407**, 2305–2327 (2010). 1004.2791.

Supplementary Information

Is appended and available in the online version of the paper.

Acknowledgments

We thank Lise Christensen and Teddy Frederiksen for advice on data reduction with the X-shooter pipeline and Maximilian Stritzinger and Rick Arendt for discussions. This investigation is based on observations made with ESO Telescopes at the La Silla Paranal Observatory under programme IDs 084.C-0315(D) and 087.C-0456(A). C.G. was supported from the NASA Postdoctoral Program (NPP) and acknowledges funding provided by the Danish Agency for Science and Technology and Innovation. G.L. is supported by the Swedish Research Council through grant No. 623-2011-7117. A.C.D.J. is supported by the Proyecto Basal PB06 (CATA), and partially supported by the Joint Committee ESO-Government Chile. The Dark Cosmology Centre is funded by the Danish National Research Foundation.

Author contributions

C.G. and J.H. conducted the observational campaign, reduced and analysed the data and wrote the manuscript. D.W. was the P.I. of the observing programs and assisted in writing the manuscript. E.D. performed calculations of vaporization radii and assisted in writing the manuscript. O.F. and G.L. assisted in data analysis. J.R.M. helped with the interpretation of the spectra and line profiles. D.M. and D.W. assisted with observations. A.C.D.J. conducted the observation of the epoch 2 spectrum. All authors were engaged in discussions and provided comments on the manuscript.

Author information

Reprints and permissions information is available at www.nature.com/reprints. The authors declare no competing financial interests. Readers are welcome to comment on the online version of the paper. Correspondence and requests for materials should be addressed to C.G. (cgall@phys.au.dk).

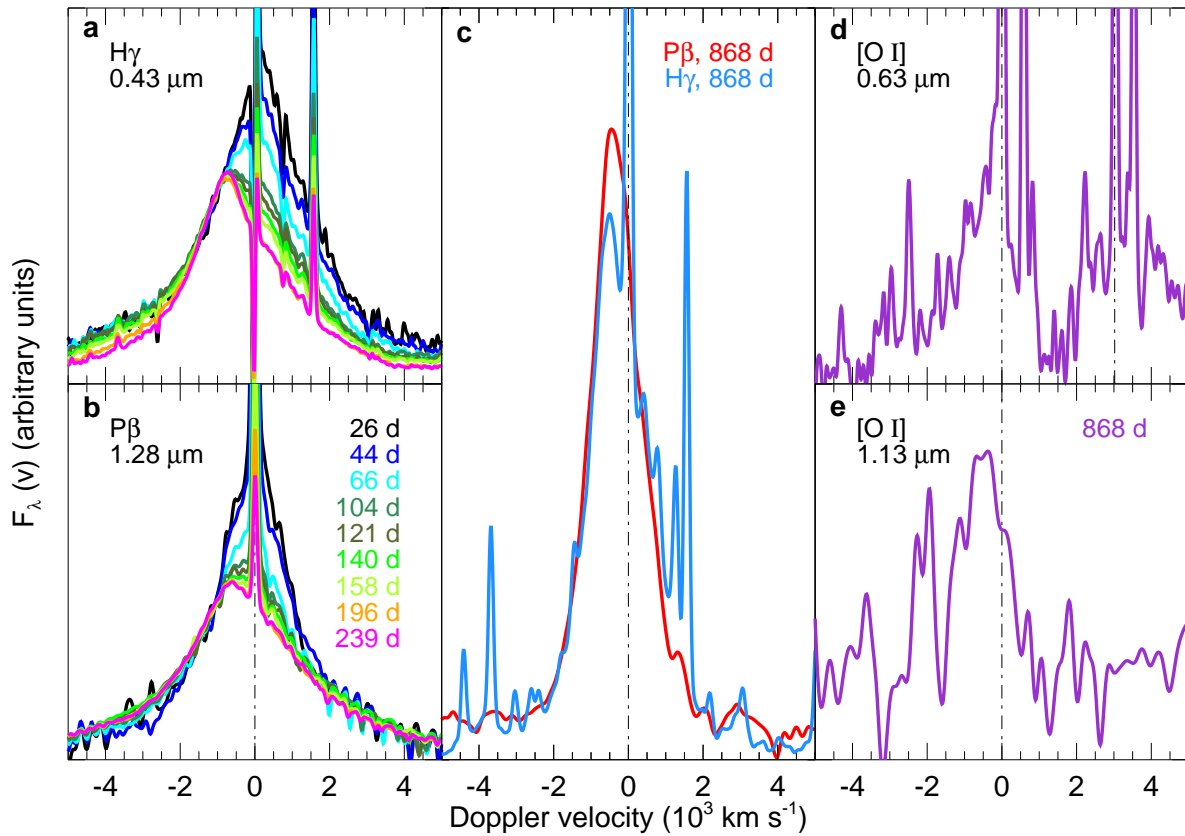


Figure 1 | Evolution of the hydrogen and oxygen line profiles in the spectrum of SN 2010jl.

Line profiles for **a**, $H\gamma$ $\lambda 4340.472$ and **b**, $P\beta$ $\lambda 12818.072$ for epochs from 26 to 239 days and **c**, $H\gamma$ and $P\beta$ at 868 days. **d**, The $[O\ I]$ $\lambda\lambda 6300.304, 6363.776$ doublet (zero velocity set at $\lambda 6300.304$), and **e**, the $[O\ I]$ $\lambda 11297.68$ line. The dashed-dotted lines in all panels denote zero velocity, at redshift $z = 0.01058$, as determined from narrow emission lines in the spectrum.

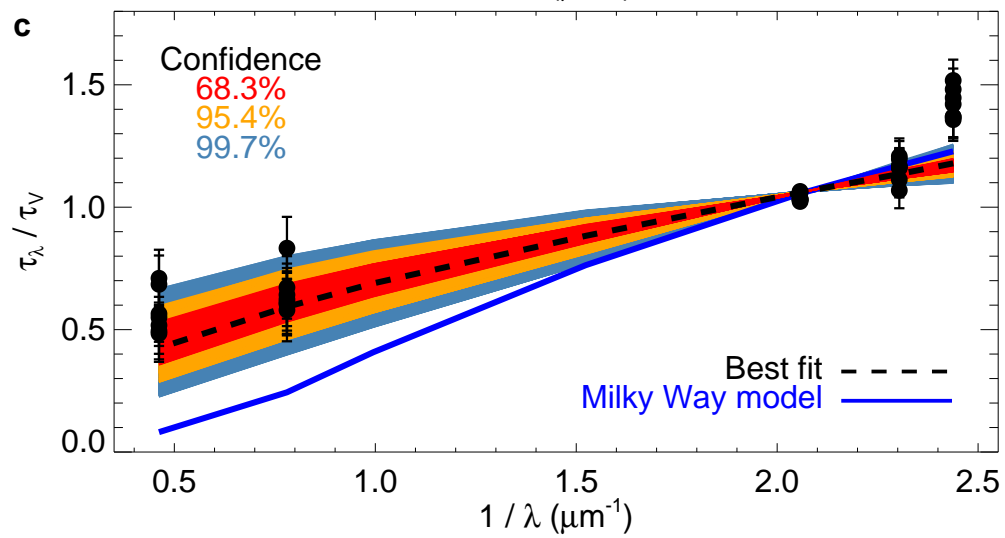
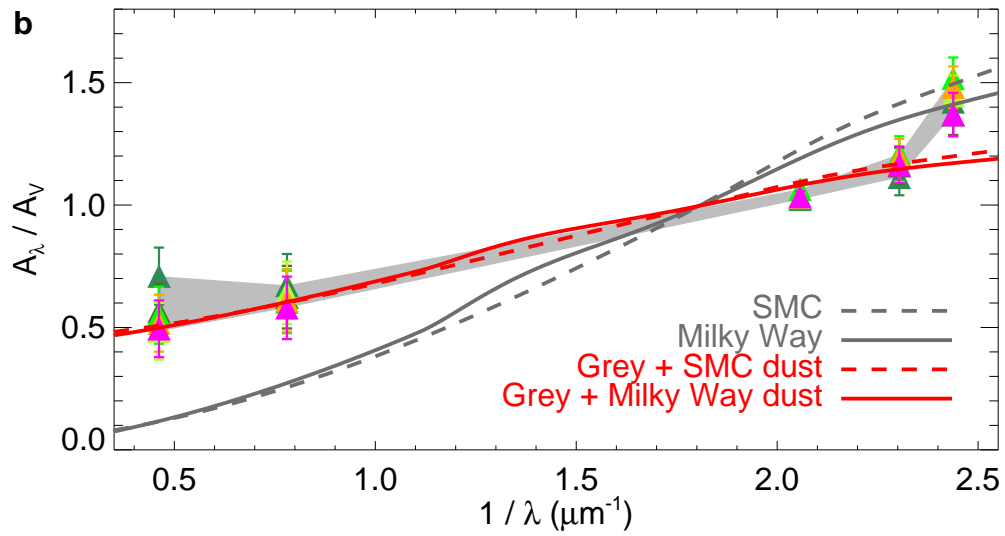
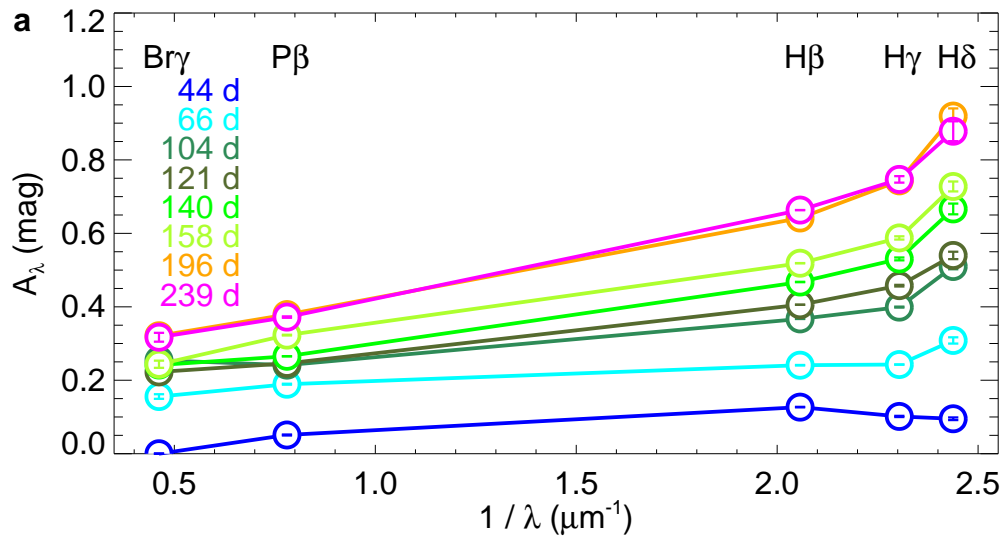


Figure 2 | Supernova dust extinction curves. **a**, The evolution of the extinction, A_λ , of the hydrogen lines (open circles with standard deviations; Methods). The solid lines represent the (linearly interpolated) extinction curves. **b**, The grey-shaded area represents the range of extinction curves relative to A_V (filled triangles with error bars). Grey curves are the SMC and MW extinction curves, while the red curves include a grey component (Methods). **c**, Fits to the optical depth within the 1, 2 and 3 σ (68.3, 95.4 and 99.7 %) confidence interval (Methods). Dashed and solid curves are models with ‘best fitting’ and MW parameters, respectively.

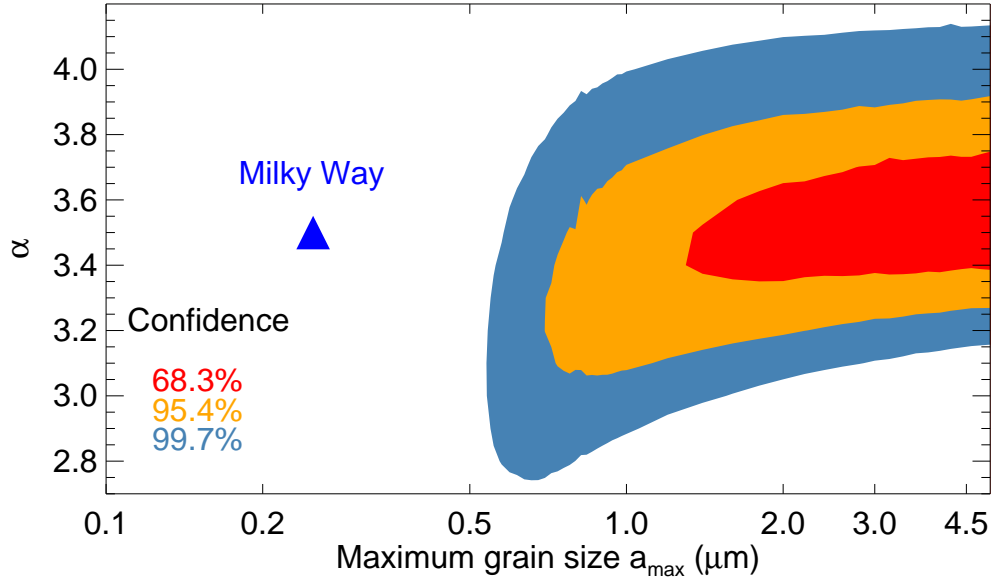


Figure 3 | Maximum grain size and slope of the grain size distribution. Confidence contours, as constrained by the normalized optical depth $\tau(\lambda)$ (see Figure 2). The most favorable power-law models lie within a parameter range for α between ~ 3.4 and 3.7 and require large grains of $a_{\max} \gtrsim 1.3 \mu\text{m}$ (1σ). The confidence limits are as in Figure 2. Even at the 3σ confidence limit the maximum grain size is larger ($a_{\max} \gtrsim 0.5 \mu\text{m}$) than MW maximum grain sizes for a power law model ($a_{\max} \approx 0.25 \mu\text{m}$) (20) or more sophisticated models (21, 22).

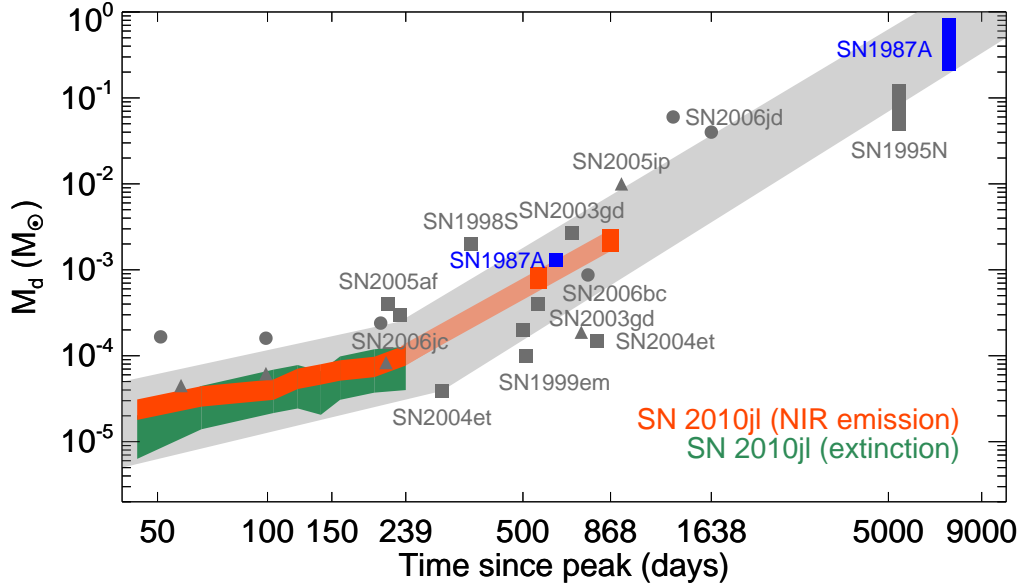


Figure 4 | Temporal evolution of the dust mass. Carbon dust masses and standard deviation derived from the extinction (green band) and the NIR emission (red bars and band; Methods) including a literature data point at 553 days (13). The light grey shaded area illustrates the evolution of the early ($M_d \propto t^{0.8}$ at $t < 250$ days) and late ($M_d \propto t^{2.4}$ at $t > 250$ days) stages of dust formation when SN 2010jl switches from circumstellar to ejecta dust formation. The grey and blue symbols correspond to literature data for SN 2005ip (triangles), SN 2006jd (dots), and other supernovae (bars) (1, 5, 6, 9, 10, 27, 30). The length of the symbols for SN 1995N and SN1987A correspond to the quoted dust mass range. For other supernova the standard deviation is either smaller than the size of the symbols or have not been reported.

Methods

We observed the Type II_n SN 2010jl in UGC 5891A at 9 epochs between 2010 November 13.4 UT and 2011 June 15.0 UT, following its discovery on 2010 November 3.5 UT (34). The SN was first detected from the All Sky Automated Survey North on 2010 October 9.6 UT and peaked on 2010 October 18.6 UT (35). The time of explosion is unknown, but we assume a time of rise to peak of ≈ 40 days. We adopt a luminosity distance of $D = 45.7$ Mpc to the SN, based on our measured redshift of $z = 0.01058$.

The observations were obtained with the X-shooter echelle spectrograph (36, 37) mounted at the Cassegrain focus of the *Kueyen* unit of the Very Large Telescope (VLT) at the European Southern Observatory (ESO) on Cerro Paranal, Chile. The X-shooter instrument allows for simultaneous spectroscopic observations in three different arms, the ultra-violet and blue (UVB), visual (VIS) and near-infrared (NIR) wavebands, covering the continuous wavelength range of 0.3–2.5 μm . The observations were performed at parallactic angle, with nodding between exposures along the 11'' slit (see Extended Data Table 1 for details). The spectra were obtained under the following conditions: clear sky and in some cases thin cirrus, average seeing of $\sim 0.8''$, and range in airmass of ~ 1.2 –2.0. For the majority of the observations we used slit widths of 1.0'' (UVB), and 0.9'' (VIS and NIR) giving resolving powers of 5,100 (UVB), 8,800 (VIS) and 5,300 (NIR), except for the second epoch on 2010 December 1.4 UT where, due to mediocre seeing conditions of $\sim 1.7''$, we used wider slit widths of 1.6'' (UVB), and 1.5'' (VIS and NIR), leading to reduced resolving powers of 3,300 (UVB), 5,400 (VIS) and 3,500 (NIR). For all epochs, observations of spectrophotometric standards were performed using a slit width of 5.0''.

We used versions 1.5.0 and 2.2.0 of the X-shooter pipeline (38) in physical mode to reduce the SN and the standard star spectra to two-dimensional bias-subtracted, flat-field corrected, order rectified and wavelength calibrated spectra in counts. To obtain one-dimensional spectra the two-dimensional spectra from the pipeline were optimally extracted (39). Furthermore the spectra were slit-loss corrected, flux calibrated and corrected for heliocentric velocities. Additionally, telluric corrections were applied. All calibration and correction procedures after the basic pipeline reduction were performed using custom IDL programs. The spectra were corrected for a Galactic extinction along the line of sight to the SN of $E(B - V)$ of 0.027 mag (40).

Two-temperature black-body fits

The progressive evolution of the supernova spectra is shown in Extended Data Figure 1. We fit the continuum emission of the early epochs (26–239 days) with a combination of two black-body functions. The first black body represents the supernova photosphere for which we infer a temperature $T_{\text{SN}} \approx 7,300$ K and a photospheric radius decreasing from $R_{\text{SN}} \sim 3.2 \times 10^{15}$ cm at 26 days to $R_{\text{SN}} \sim 2.4 \times 10^{15}$ cm at 239 days. The second black-body function accounts for the NIR excess noticeable in the spectra, which we attribute to dust emission.

To properly fit the hot dust emission we therefore use a modified black-body function. The fit to the spectra is computed as

$$F_{\nu}(\nu) = B_{\nu}(\nu, T_{\text{SN}}) R_{\text{SN}}^2 / D^2 + N_{\text{d}} / D^2 \int_{a_{\text{min}}}^{a_{\text{max}}} f(a) m(a) \kappa_{\text{abs}}(\nu, a) B_{\nu}(\nu, T_{\text{hot}}) da, \quad (1)$$

where $B_{\nu}(\nu, T)$ is the Planck function at temperature $T = T_{\text{SN}}$ for the supernova and $T = T_{\text{hot}}$ for the dust, R_{SN} is the radius of the supernova photosphere, D is the luminosity distance to the supernova,

N_d is the total number of dust particles, $m_d(a) = (4\pi/3)\rho a^3$ is the mass of a single dust grain of radius a and $\kappa_{\text{abs}}(\nu)$ is the dust mass absorption coefficient for an assumed dust composition, i.e., amorphous carbon (41) and silicates (42). The mass density is $\rho = 1.8 \text{ g cm}^{-3}$ for amorphous carbon and $\rho = 3.3 \text{ g cm}^{-3}$ for silicates. We use a power-law grain size distribution function $f(a) \propto a^{-\alpha}$, which is normalized to unity in the interval $[a_{\text{min}}, a_{\text{max}}]$ as $\int_{a_{\text{min}}}^{a_{\text{max}}} f(a) da = 1$.

Extended Data Figure 2 depicts supernova spectra obtained at 44 days, 196 days and at a late epoch of 868 days. The adopted grain size distribution assumes the parameters α , a_{min} and a_{max} from the ‘best fitting’ amorphous carbon model obtained from the extinction curves (Figures 2 and 3). To fit the spectrum at 868 days we exchanged the SN black-body with a power law for the host galaxy continuum emission as $C_{\text{norm}} \nu^{-1.24}$, where C_{norm} is a normalization constant and the power law exponent resulted from the fit. Additionally, for this epoch we explored two dust compositions, i.e., amorphous carbon and silicates, and models with single grain sizes a between 0.001 and 5.0 μm , as well as grain size distribution models varying α between 2.0 and 4.5. We found that (1) amorphous carbon single grain size models as well as grain size distribution models prefer large grains (1–5 μm), (2) the quality of the fits of silicate models is fairly insensitive to the size of the grains and can accommodate small grains, (3) we are unable to produce models with temperatures less than $\sim 1,000 \text{ K}$, (4) the inferred dust masses for silicate grains are typically up to an order of magnitude higher than for amorphous carbon. All spectra are well fit by a supernova temperature $T_{\text{SN}} \approx 7,300 \text{ K}$ and a dust temperature, T_{hot} , which decreases from $\approx 2,300 \text{ K}$ to 1,600 K during the first 239 days, down to $\approx 1,100 \text{ K}$ at 868 days.

Extended Data Figure 1 also shows *Spitzer*/IRAC 3.6 μm and 4.5 μm observations (11). We

can fit the $3.6\ \mu\text{m}$ data point with the same modified black-body model as used for the other epochs (grey dotted curve in Extended Data Figure 1).

Analysis of line profiles

The spectra exhibit a richness of emission lines on top of the continuum, featuring in particular hydrogen and helium lines which are: $\text{H}\delta\ \lambda 4101.734$, $\text{H}\gamma\ \lambda 4340.472$, $\text{H}\beta\ \lambda 4861.35$, $\text{He I}\ \lambda 5875.621$, $\text{H}\alpha\ \lambda 6562.79$, $\text{He I}\ \lambda 7065.2578$, $\text{P}\delta\ \lambda 10049.8$, $\text{He I}\ \lambda 10830.199$, $\text{P}\gamma\ \lambda 10938.17$, $\text{P}\beta\ \lambda 12818.072$ and $\text{Br}\gamma\ \lambda 21655.268$. The lines have a narrow ($\sim 100\ \text{km s}^{-1}$) velocity component on top of an intermediate width velocity component. For $\text{H}\delta$, $\text{H}\gamma$, $\text{H}\beta$, $\text{H}\alpha$, $\text{He I}\ \lambda 5875.621$ and $\text{He I}\ \lambda 10830.199$ the narrow lines exhibit a characteristic P Cygni profile (i.e., a blueshifted absorption and redshifted emission component).

Only a subset of the hydrogen lines are suitable for quantitative extinction studies. We require that the lines exhibit a clear single peaked intermediate velocity component across all epochs which can be well represented by a Lorentzian profile, not necessarily centred at the zero velocity (Extended Data Figure 3a). None of the He I lines are suitable for extinction studies because they show conspicuous bumps in the wings. Moreover, the wings significantly broaden with time (Extended Data Figure 3b). The He I $\lambda 10830.199$ line is blended with the P γ $\lambda 10938.17$ line, ruling out both lines for our studies. The P δ $\lambda 10049.8$ line is located at the cross-over between the X-shooter VIS and NIR arms giving rise to unreliable flux calibration and background subtraction.

Some lines show the presence of large velocities. Extended Data Figure 4 shows $\text{H}\beta$ P Cygni profiles featuring velocities up to $\sim 20,000\ \text{km s}^{-1}$ which arise from the fast expanding thin outer

layers of the supernova ejecta. The bulk expansion velocity of the supernova ejecta (corresponding to the minimum of the P Cygni profile) is around $7,500 \text{ km s}^{-1}$. Other lines, e.g., $\text{H}\alpha$, are characterized by an underlying broad velocity component. As shown in Extended Data Figure 5a, we can fit the 26 day $\text{H}\alpha$ line with a combination of a broad Gaussian with a full width of half maximum of $\sim 5,000 \text{ km s}^{-1}$ and an intermediate Lorentzian with HWHM $\sim 860 \text{ km s}^{-1}$ centred at zero velocity. While the $\text{H}\alpha$ line is often used to demonstrate the effect of dust attenuation of the red wing (43), it is discarded for our study because of the progressive broadening of the wings (Extended Data Figure 3b), which prevents a straightforward quantitative analysis.

At 868 days the emission lines no longer exhibit a broad velocity component. The intermediate velocity components of the hydrogen emission lines feature velocities up to $\sim 2,000\text{--}3,000 \text{ km s}^{-1}$ similar to the oxygen $[\text{O I}] \lambda 6300.304$ and $[\text{O I}] \lambda 11297.68$ lines (Figure 1). The lines are not well represented by Lorentzian profiles (Figure 1, middle panel). Consequently, the late epoch is not considered for our quantitative extinction studies.

From single Lorentzians fits to $\text{H}\delta$, $\text{H}\gamma$, $\text{H}\beta$, $\text{P}\beta$ and $\text{Br}\gamma$, we estimated the Lorentzian HWHM of the intermediate velocity components of these lines (about $1,500 \pm 200 \text{ km s}^{-1}$). Extended Data Figure 5b shows that the hydrogen lines (e.g., $\text{H}\beta$) exhibit deviations from symmetry, despite being adequately represented by Lorentzian profiles for our purposes (Extended Data Figure 3a). We also measured the blueshifts of the peaks (Extended Data Figure 6).

To obtain the hydrogen line profiles (Figure 1), the spectrum from each epoch was continuum subtracted and scaled to the first epoch. The scaling was set by the velocity at which the blue

side of the line changed from being extinguished to being unextinguished (between $-1,200$ to $-1,000 \text{ km s}^{-1}$). This ensures that we measure only the extinguished parts of the lines. The blue unextinguished wings from all epochs coincide. At the late epoch (868 days), $\text{H}\gamma$ was scaled to $P\beta$ at a velocity of -800 km s^{-1} .

Extinction measurements

Attributing the red depressions to dust, we calculated the extinction (Figure 2a) from the fitted Lorentzian profiles as $A_\lambda = -2.5 \log(I(\lambda, t)/I_{\text{ref}}(\lambda))$, where $I(\lambda, t)$ is the line profile integrated over a velocity range extending from the scaling velocity up to $4,000 \text{ km s}^{-1}$ and $I_{\text{ref}}(\lambda)$ is the integrated line profile from the first epoch which was taken as a reference. We obtained the error bars of A_λ (standard deviations) using Monte Carlo calculations by varying the fit parameters of the Lorentzian line profiles within their uncertainties. The error bars reflect the signal to noise ratio of the lines and the extent to which they are well represented by Lorentzians. From measurements of A_V ($\lambda_V = 5,505 \text{ \AA}$) and $E(B - V)$ in Figure 2, we directly infer $R_V = A_V/E(B - V) \approx 6.4$. The wavelength dependent optical depth is fit with (1) a phenomenological model based on grey dust plus either a SMC or MW dust, $A_{\text{SMC, MW}}(\lambda)$, as $A_\lambda = A_{\text{grey}} + A_{\text{SMC, MW}}(\lambda)$ (Figure 2b) and (2) a single dust model, i.e., only carbon dust, which for a shell is,

$$\tau(\lambda) = \frac{N_d}{4 \pi R^2} \int_{a_{\text{min}}}^{a_{\text{max}}} f(a) m_d(a) \kappa_{\text{ext}}(\lambda, a) da, \quad (2)$$

where R is the distance of the cool dense shell (CDS) from the SN and $\kappa_{\text{ext}}(\lambda, a)$ is the mass absorption coefficient, i.e., for amorphous carbon (41). We calculate a grid of models varying the slope α between 0.5 and 4.5, and the lower and upper limits of the grain size distribution,

a_{\min} and a_{\max} , between 0.001 and 5.0 μm ($a_{\min} < a_{\max}$). The dispersion of the normalized data (between day 66–239) is added to the error (Figure 2c). We used the chi-square (χ^2) minimization method to determine the best fitting parameters α and a_{\max} of the grain size distribution function, for fixed $a_{\min} = 0.001 \mu\text{m}$ (Figure 3). The χ^2 value for a desired confidence limit p is calculated as $\chi^2 = \chi_{\min}^2 + \Delta\chi^2(p)$, where χ_{\min}^2 is the global minimum χ_{\min}^2 value of all models. The best fitting model is characterized by $\alpha = 3.6$, $a_{\min} = 0.001 \mu\text{m}$ and $a_{\max} = 4.2 \mu\text{m}$. However, our models cannot account for the upturn towards $\text{H}\delta$ (Figure 2b), which we attribute to a systematic effect caused by intrinsic line changes rather than to small grains. We note that the considered grain radius is truncated at 5 μm beyond which the size parameter, $x = 2\pi a/\lambda$, becomes prohibitively large making mass absorption coefficient calculations difficult.

Lightcurves

In Extended Data Figure 7a we show synthetic UVBRI optical and JHK NIR lightcurves generated from our X-shooter spectra compared to broad band photometry from the literature (13) (we have added 1.4 mag to the published U band magnitudes, which happens to be twice the U band AB offset). It is evident that there is good agreement giving credence to the flux calibration of our spectra. The energy input (Extended Data Figure 7b) from ^{56}Co was normalized to the total observed luminosity on day ~ 26 , and the ^{44}Ti contribution was calculated assuming a relative Co/Ti yield (by number) of 3×10^{-4} (44). The UVO and NIR luminosities (Extended Data Figure 7a) are derived from the black body fits to our X-shooter spectra. A power-law approximation to the UVO luminosity shows that it decays as a $t^{-0.4}$ power-law.

Dust heating and vaporization

A dust grain of radius a located at a distance R from the SN will attain an equilibrium temperature, T_d , determined by the balance between the rate it is heated by the SN and its cooling rate by NIR emission. The equation describing this balance is given by

$$\int_0^\infty \pi a^2 Q_{\text{abs}}(\nu, a) \left(\frac{L_\nu(\nu)}{4\pi R^2} \right) d\nu = \int_0^\infty 4\pi a^2 Q_{\text{abs}}(\nu, a) \pi B_\nu(\nu, T_d) d\nu. \quad (3)$$

The SN will vaporize a grain when its temperature exceeds the vaporization temperature. We take $T_{\text{vap,SIL}} = 1,500$ K for silicates. Due to the large uncertainty in $T_{\text{vap,AC}}$ for amorphous carbon grains we adopt a temperature range of 2,000–3,000 K.

The SN light is preceded by a short ($\Delta t \lesssim 1$ d) burst of radiation as the shock, resulting from the core collapse, breaks out of the stellar surface (45). From direct observations (46, 47) of such a shock breakout and models to fit early UV optical lightcurves (48, 49) a shock breakout burst typically lasts of order 100–1000 seconds with peak luminosities of around $10^{12} L_\odot$ and effective temperatures of a few times 10^5 K after which the luminosities decrease in less than one day by over a few orders of magnitudes. A short burst of radiation characterized by a 10^5 K black body and a luminosity of $10^{11} L_\odot$, similar to that inferred for Cas A (50), will vaporize any pre-existing dust in the circumstellar material (CSM), creating a dust-free ‘cavity’ of radius R_{cav} . Extended Data Figure 8a shows that, independently of the grain species, small grains are vaporized out to larger distances from the SN than large grains. For silicate grains, R_{cav} is about twice as large as for carbon grains. As a consequence of shock breakout, no dust grains can exist out to R_{cav} of about 10^{17-18} cm.

Any dust that may subsequently form within the radius R_{cav} will be subjected to the SN light, characterized by a 7,300 K black body and a luminosity of $\sim 5 \times 10^9 L_{\odot}$. Extended Data Figure 8b shows the vaporization radii, R_{vap} , for the observed SN luminosity at the first epoch (26 days past peak). Independently of grain size, the R_{vap} for silicates is significantly larger than R_{vap} for amorphous carbon at any assumed $T_{\text{vap,AC}}$ and CDS radius, which is about 2×10^{16} cm at this epoch (Supplementary Information, Extended Data Figure 9b). Dust grains of sizes around 0.05–0.1 μm have the largest vaporization radii for either dust species. It is evident that only amorphous carbon grains can survive the radiation from the underlying SN at the location of the CDS. Amorphous carbon grains with grain sizes $\gtrsim 0.25 \mu\text{m}$ have temperatures ($\lesssim 2,200$ K), consistent with the hot dust temperatures inferred from the modified black-body fits to the NIR emission (Extended Data Figure 8c). These grain radii are consistent with those inferred from our extinction measurements. The small carbon grains ($\lesssim 0.25 \mu\text{m}$), which are required to explain the observed UV extinction (see Figure 2), have higher temperatures (2,200–2,700 K) but do not contribute strongly to the NIR emission. Silicate grains cannot exist at the location of the CDS.

Dust mass estimates

The dust mass is derived from either the extinction or the NIR emission as

$$M_{\text{d}} = N_{\text{d}} \int_{a_{\text{min}}}^{a_{\text{max}}} f(a) m_{\text{d}}(a) da. \quad (4)$$

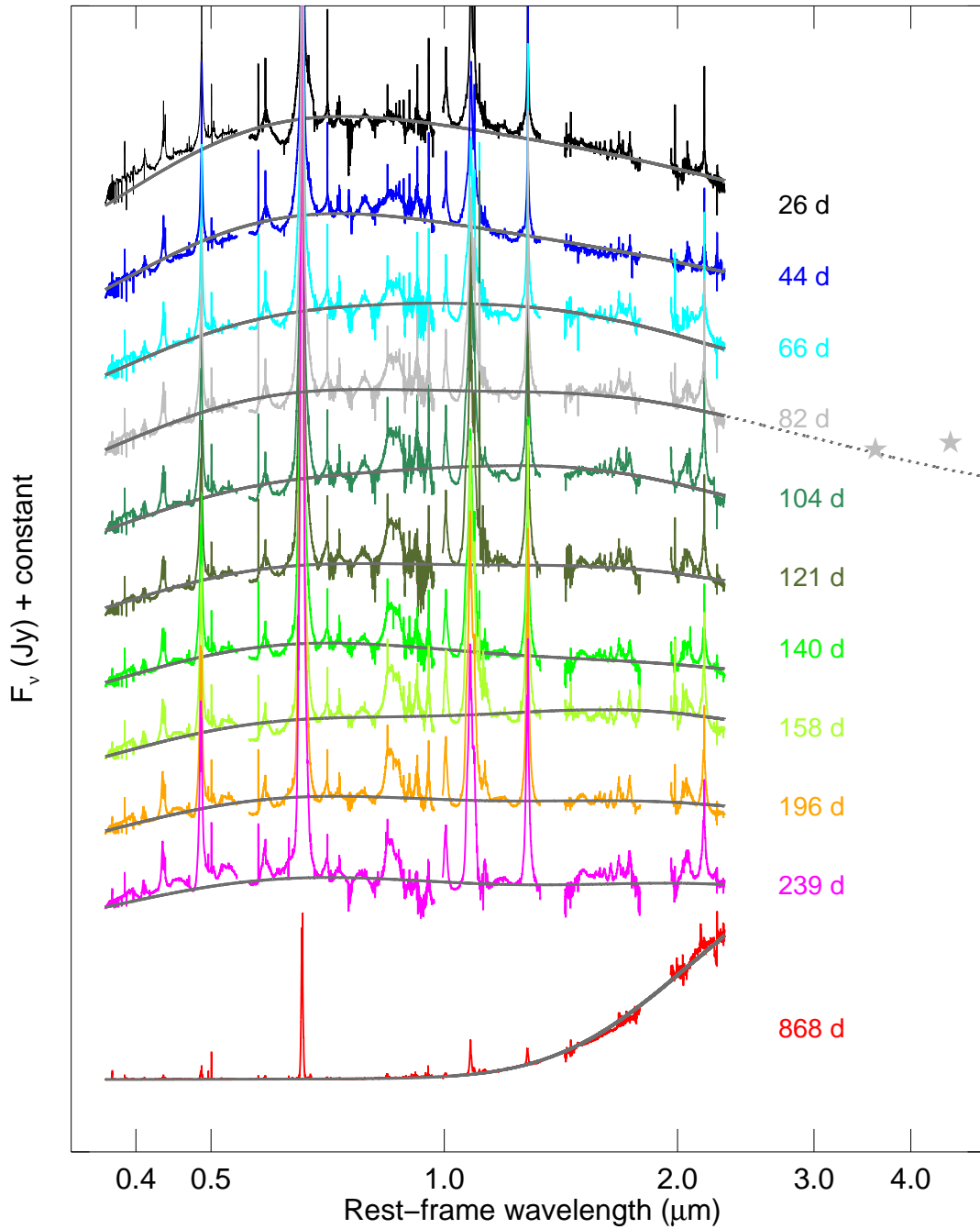
The total number of dust particles N_{d} is obtained from the fits using either Equations (1) or (2).

In Figure 4 we display the evolution of the carbon dust masses, which are derived from (1) the extinction and its standard deviation obtained for the best fitting grain size distribution (Figures 2

and 3) at $R_{\text{CDS}} = 2.0 \times 10^{16}$ cm and (2) the NIR emission, varying α between 3.5 and 3.7. A power law fit, $M_{\text{d}} \propto t^{\beta}$, to the dust mass evolution at early and late phases shows a slow increase ($\beta = 0.8$) at early times and accelerated build up of the dust mass ($\beta = 2.4$) after 239 days. The estimated carbon dust mass of $\approx 2 \times 10^{-3} M_{\odot}$ at the late epoch is most likely a lower limit (Supplementary Information).

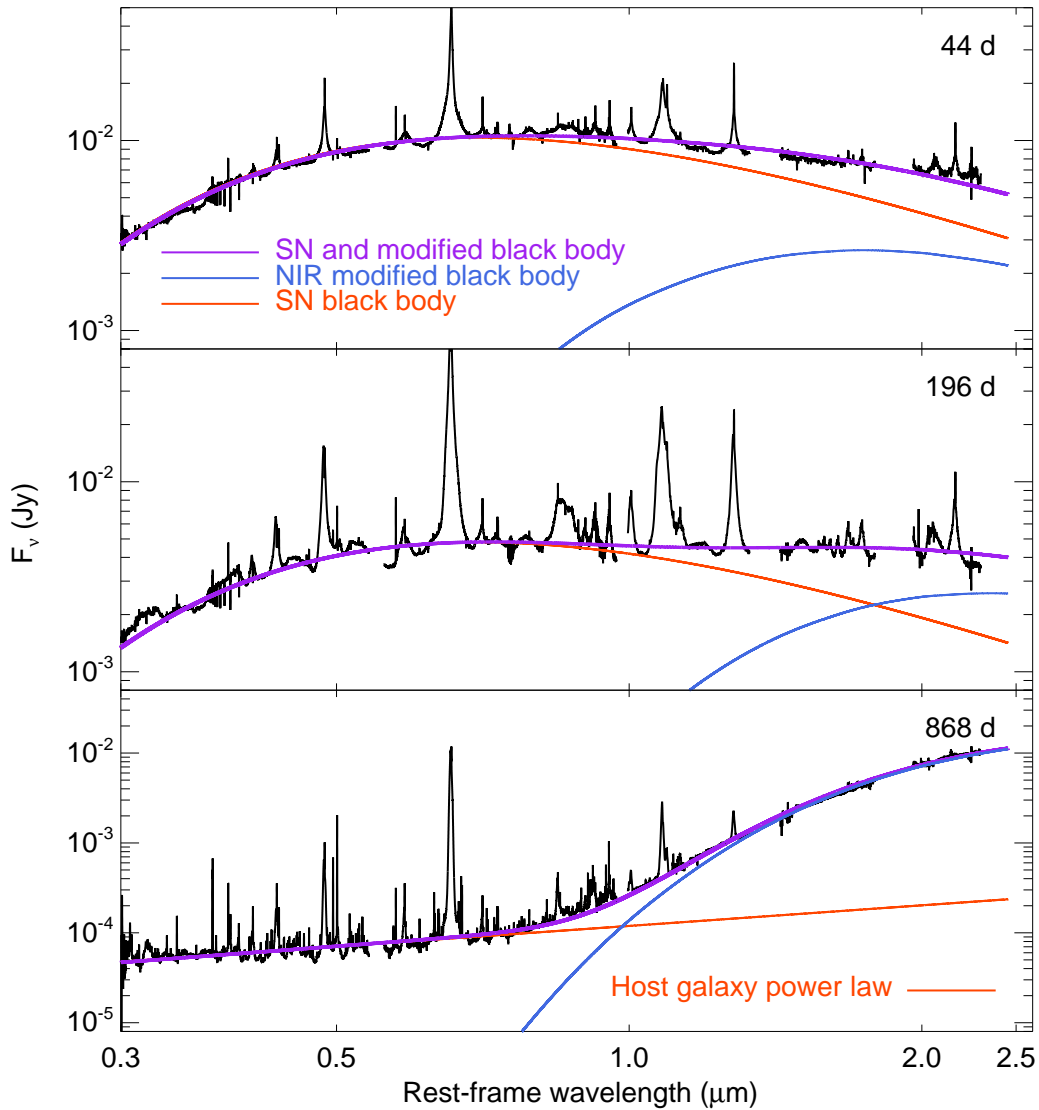
Extended Data Figure 9a visualises the sensitivity of the inferred extinction dust mass to a_{max} and α . Carbon dust masses at 239 days past peak are calculated and displayed for parameters within the 3σ confidence interval (see Figure 3) and for fixed $a_{\text{min}} = 0.001 \mu\text{m}$. Large grains exhibit a stronger dependency on α , with larger dust masses being reached for small α (i.e., favouring large grains). For small grains the dust mass is almost independent of α . For large α the dust mass remains independent of a_{max} for large grains whereas for small α , the dust mass increases steeply with increasing a_{max} .

Requiring that the extinction and emission dust mass originate from the CDS, the allowed location of the CDS is constrained by $R_{\text{vap}} \lesssim R_{\text{CDS}} \lesssim R_{\text{shock}}$ (Extended Data Figure 9b). The location of the forward shock, R_{shock} , at day 239 is estimated assuming a velocity of $3.5 \times 10^4 \text{ km s}^{-1}$ until 26 days past peak and $3,000 \text{ km s}^{-1}$ for the subsequent 213 days.

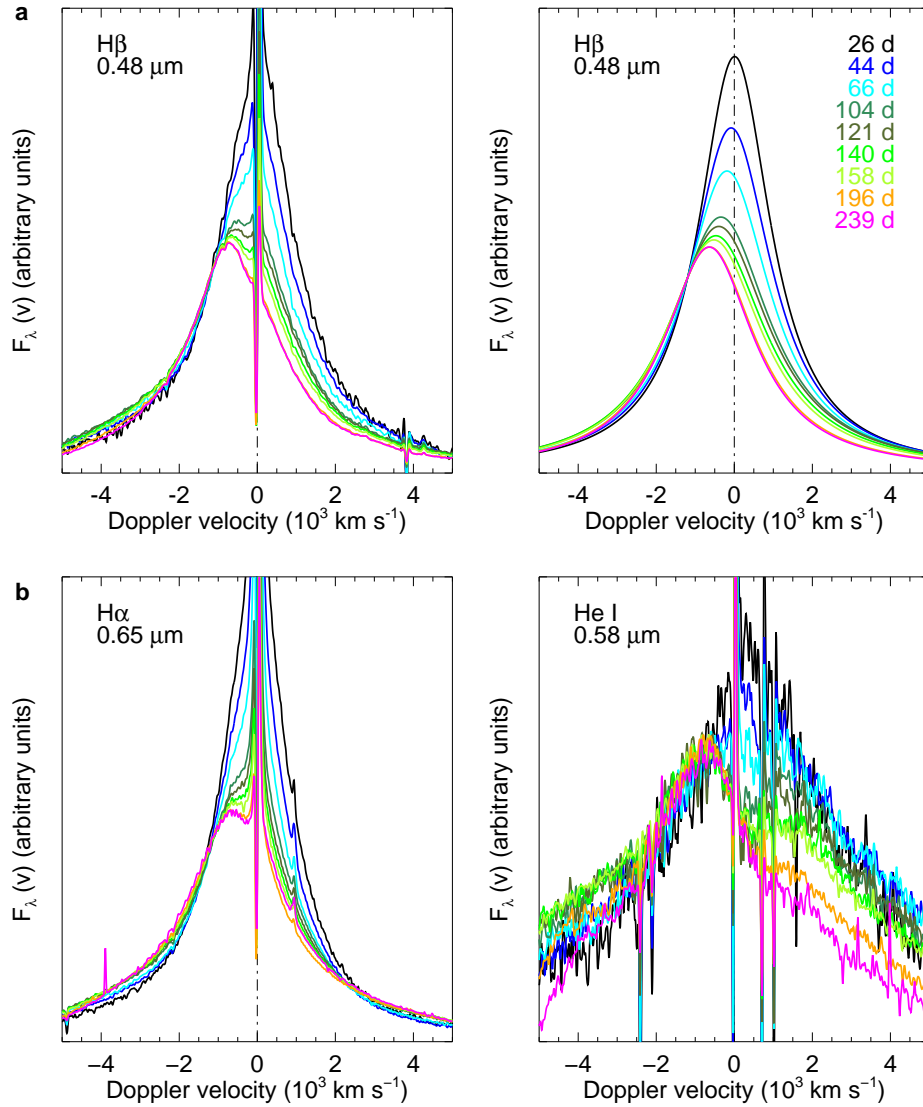


Extended Data Figure 1 | Time sequence of the supernova spectra. Spectra from ten epochs between $t = 26$ and 868 days past peak. The spectra are offset by an arbitrary constant. The atmospheric telluric bands at $1.33\text{--}1.43 \mu\text{m}$ and $1.79\text{--}1.96 \mu\text{m}$ have been excluded as well as the

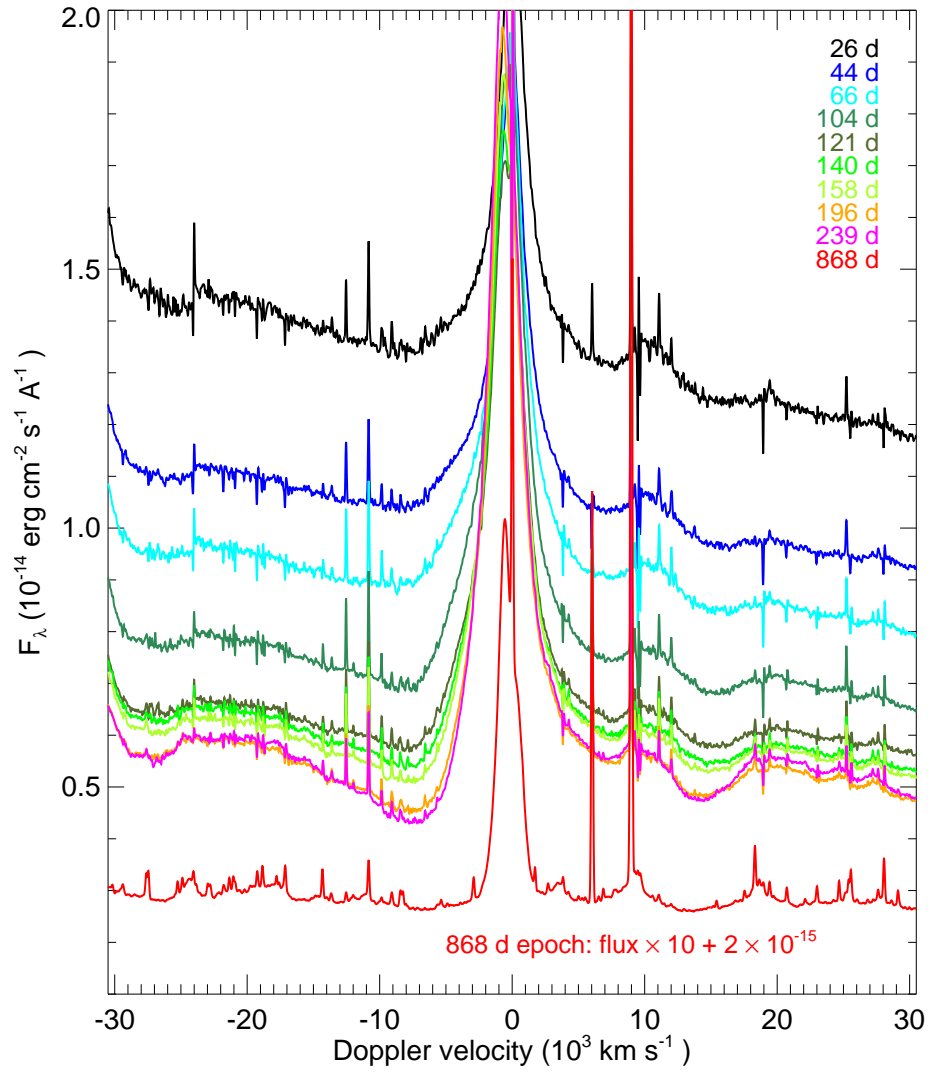
dichroic gaps between the X-shooter instrument arms at $0.54\text{--}0.56\ \mu\text{m}$ and $0.97\text{--}0.995\ \mu\text{m}$. The light grey spectrum is an interpolated spectrum at the epoch of observations of the IRAC $3.6\ \mu\text{m}$ and $4.5\ \mu\text{m}$ data (grey stars) (11). The solid grey curves are fits to the spectra, composed of multiple distinct black-body functions.



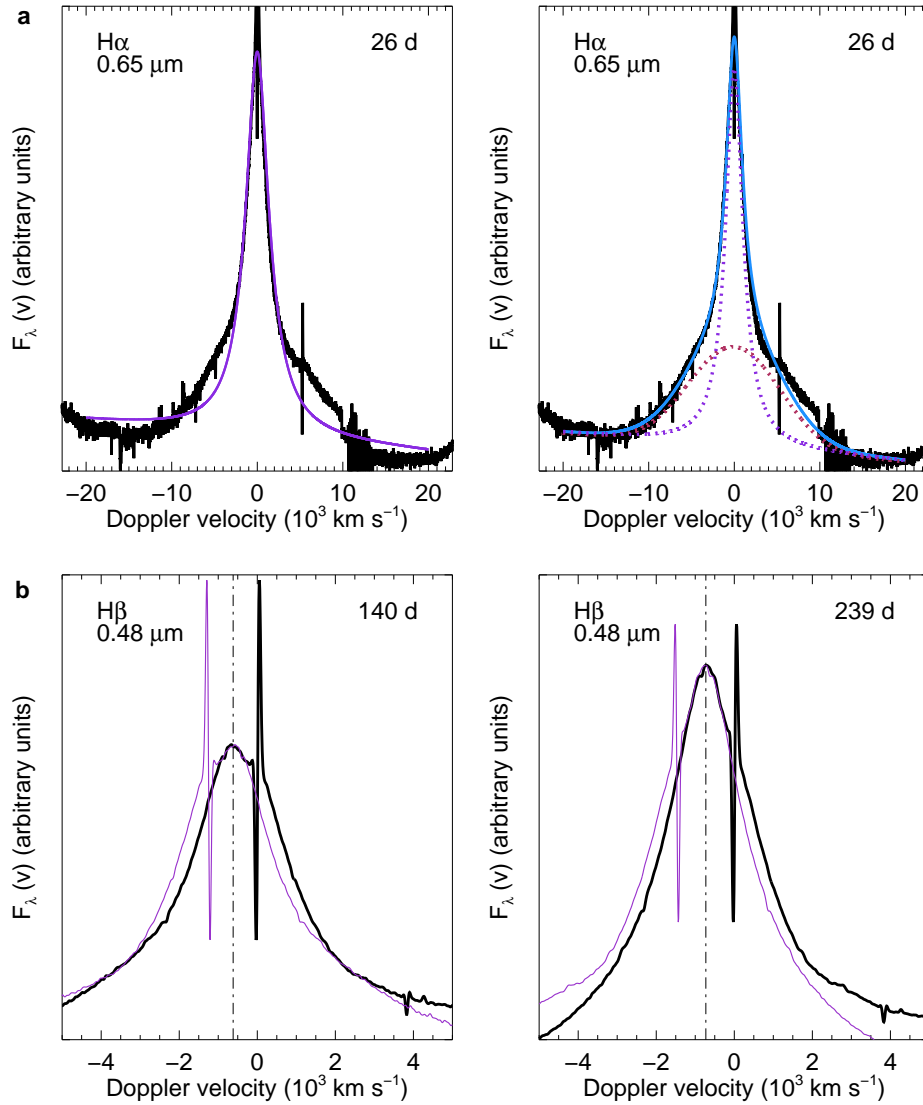
Extended Data Figure 2 | NIR excess dust emission in supernova spectra at three different epochs. The spectral shape of the supernova shows little evolution for the early epochs (44 and 196 days past peak). The late epoch at 868 days exhibits strong NIR emission while the supernova continuum has faded. The atmospheric telluric bands at $1.33\text{--}1.43\ \mu\text{m}$ and $1.79\text{--}1.96\ \mu\text{m}$ as well as the dichroic gaps of the X-shooter instrument arms at $0.54\text{--}0.56\ \mu\text{m}$ and $0.97\text{--}0.995\ \mu\text{m}$ have been excluded.



Extended Data Figure 3 | Line profiles. a, Comparison of the observed line profile (left panel) to the line profile of the Lorentzian line fits (right panel), illustrated for H β λ 4861.35. **b**, Left panel: Line profile of the H α λ 6562.79 line. The progressive broadening of the line causes both the blue and red wings to cross at different epochs. Right panel: The line profile of the He I λ 5875.621 line exhibits a similar effect. The lines increasingly deviate from a Lorentzian profile.

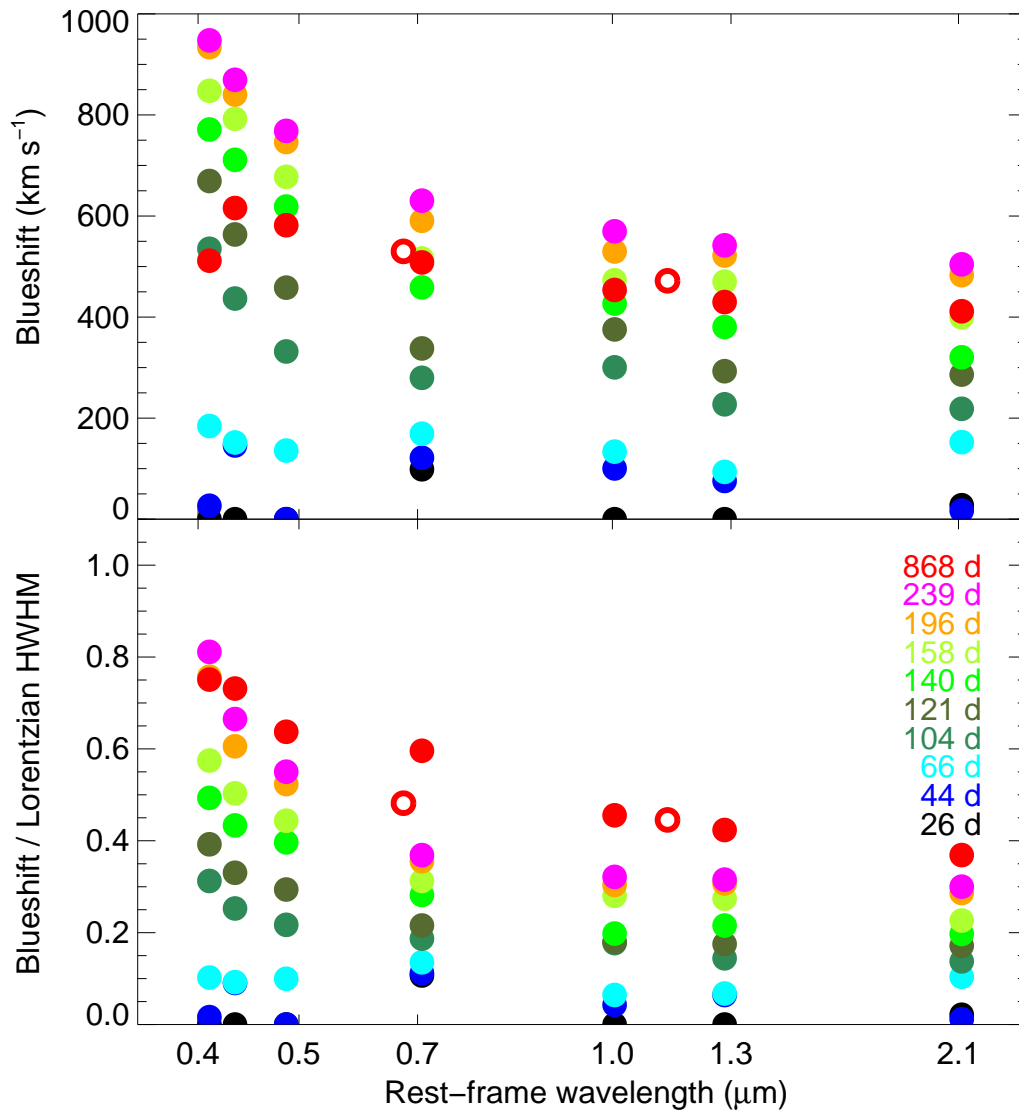


Extended Data Figure 4 | Development of the broad P Cygni profile of H β . Within the early epochs (< 239 days) the hydrogen emission line H β $\lambda 4861.35$ develops a strong P Cygni profile. The minimum of the P Cygni profile is at $\sim 7,500$ km s $^{-1}$. The largest velocities associated with the P Cygni profile are at $\approx 20,000$ km s $^{-1}$. The late epoch (868 days) has been scaled by a factor 10 and offset for better comparison to the early epochs. The H β line no longer exhibits features of high velocities. The wings of the intermediate velocity component extend to $\sim 2,000$ – $3,000$ km s $^{-1}$.



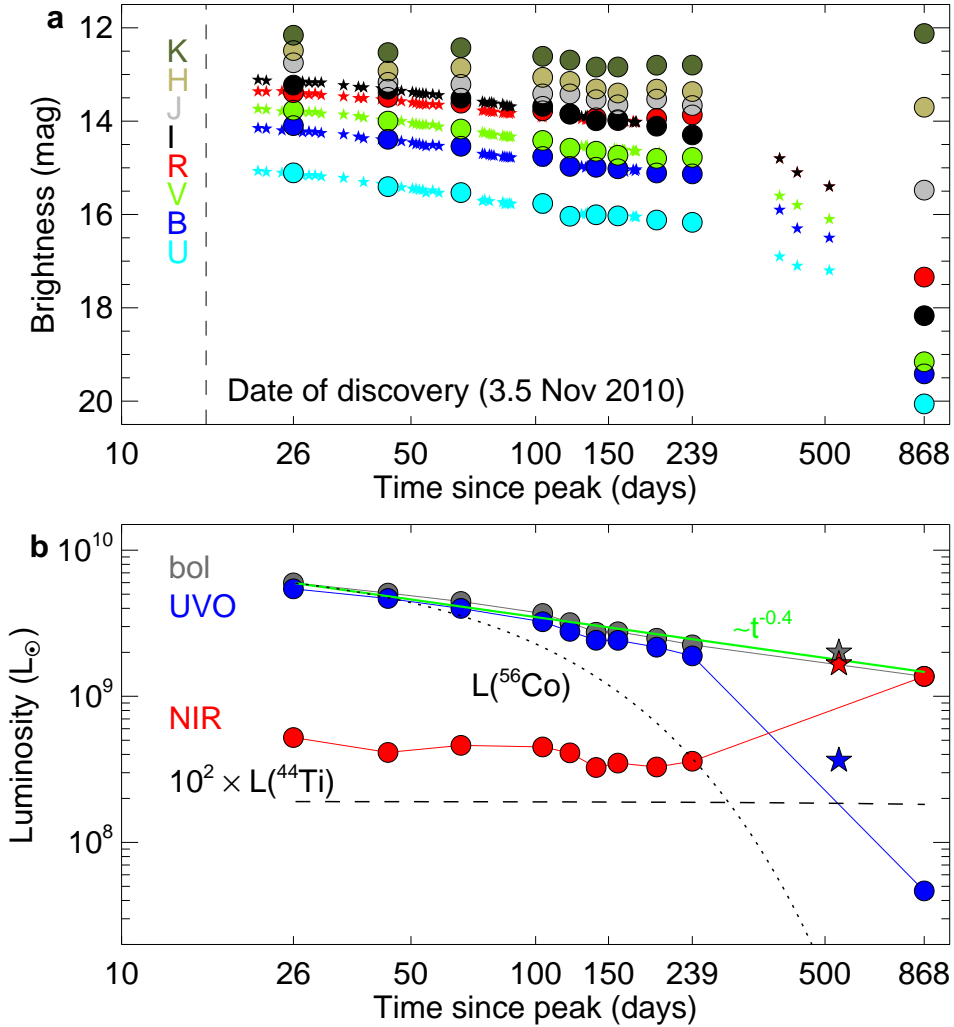
Extended Data Figure 5 | Velocity components and asymmetry of the intermediate emission

lines. **a**, Left panel: The H α λ 6562.79 line cannot be fit with a single Lorentzian (purple solid curve). Right panel: The broad (pink dotted curve) and the intermediate velocity component (purple dotted curve) and the combination of the two (blue solid curve). **b**, The H β λ 4861.35 line is asymmetric with respect to its peak velocities (~ -458 km s $^{-1}$ at 140 days and ~ -768 km s $^{-1}$ at 239 days). The mirrored emission lines are shown as purple thin curves. The mirror axis is shown as black dashed-dotted curve. Similar effects are seen for other emission lines.

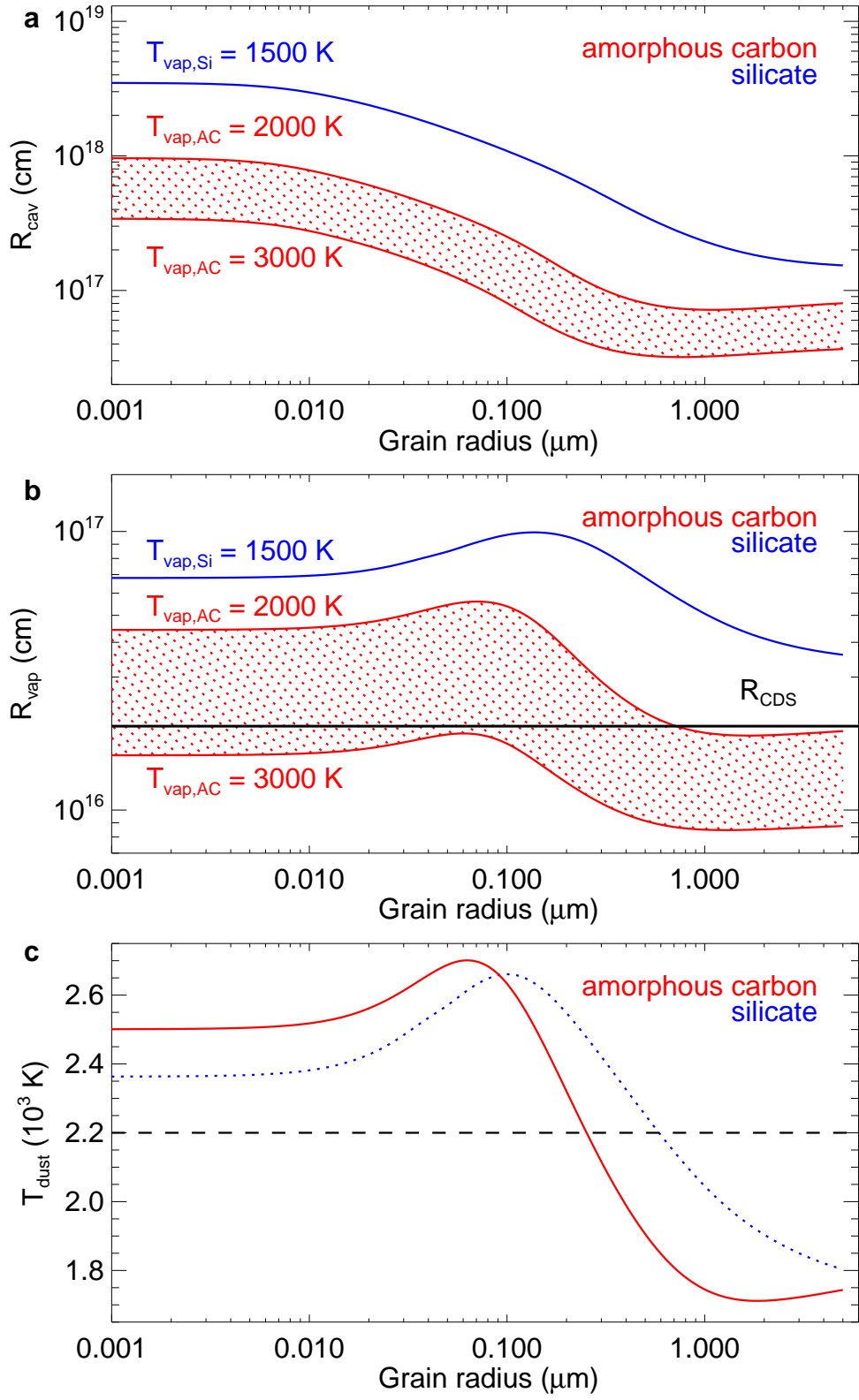


Extended Data Figure 6 | Evolution of the blueshift velocity of hydrogen and metal lines.

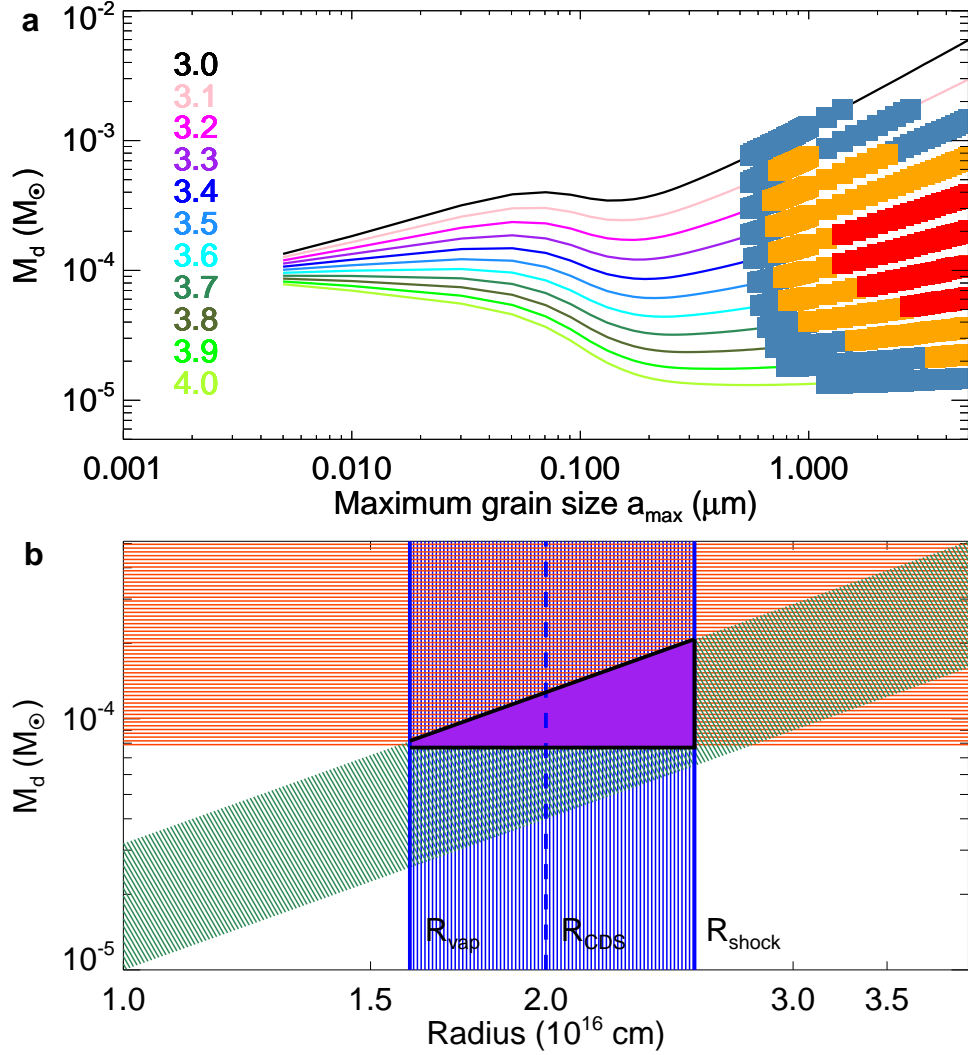
The blueshift of the hydrogen lines is wavelength dependent and increases with time for the early epochs. At any epoch the blueshift is smaller for lines at longer wavelengths. The filled symbols correspond to the blueshifts of the hydrogen emission lines and the open circles correspond to the oxygen lines. The blueshift to HWHM ratio for the early epochs resembles the extinction curves (Figure 2).



Extended Data Figure 7 | Lightcurves. **a**, Synthetic UVBRI and JHK lightcurves (filled circles) compared to the UBVRI optical photometry of (Ref. 13) (small stars). **b**, Energy output. The temporal evolution of the UVO and NIR luminosities (blue and red symbols, respectively) and the total bolometric (UVO + NIR) luminosity (black diamonds). The green curve is a $t^{-0.4}$ power-law approximation to the UVO emission at early times. We have included data points from the literature (filled stars) at 553 days (13). The maximum possible contributions to the heating of the ejecta from the radioactively decaying ^{56}Co and the isotope ^{44}Ti are shown as a dotted curve and a dashed line, respectively.



Extended Data Figure 8 | Dust vaporization radii and temperatures as a function of grain radius. **a**, Radii, R_{cav} , from an initial burst of radiation. **b**, Radii, R_{vap} , from the observed supernova luminosity at 26 days. R_{cav} and R_{vap} depend on the vaporization temperatures $T_{\text{vap,AC}}$ and $T_{\text{vap,Si}}$. The black line indicates the location, R_{CDS} , of the CDS. **c**, The dust temperatures at R_{CDS} , for grains heated by the supernova light and cooled through the NIR emission. The dashed line indicates T_{hot} derived from the spectral fits (26 days). Amorphous carbon grains (solid curve) have temperatures $\lesssim T_{\text{vap,AC}}$. Silicate grains (dotted curve) would be hotter than $T_{\text{vap,Si}}$ and therefore cannot exist.



Extended Data Figure 9 | Dust mass at 239 days past peak. a, Sensitivity of the dust mass to the parameters a_{\max} (coloured curves) and α of the grain size distribution function. The filled coloured squares represent the dust masses for the parameters of the grain size distribution function of the 1σ (red), 2σ (orange) and 3σ (blue) confidence interval (Figures 2c and 3). **b**, The extinction dust mass and its standard deviation (green-shaded band), the dust mass from the NIR emission (red-shaded band) and the radius range $R_{\text{vap}} \lesssim R_{\text{CDS}} \lesssim R_{\text{shock}}$ (blue lines and shaded area). The overlapping region (purple framed area) of the three bands constrains R_{CDS} and the dust mass.

Date (UT)	Airmass	Seeing (")	Exposure times (s)			Days past peak on 2010 Oct 18.6 UT
			UVB	VIS	NIR	
2010 Nov 13.4	1.53	0.91	2×100	2×100	2×100	26
2010 Dec 1.4	1.25	1.74	2×250	2×250	8×100	44
2010 Dec 23.3	1.22	1.52	2×250	2×250	8×100	66
2011 Jan 30.3	1.21	1.05	2×250	2×250	8×100	104
2011 Feb 16.1	1.34	0.87	2×250	2×250	8×100	121
2011 Mar 7.2	1.24	0.77	2×250	2×250	8×100	140
2011 Mar 25.1	1.21	0.98	2×400	2×450	10×100	158
2011 May 3.0	1.21	0.74	2×400	2×450	10×100	196
2011 Jun 15.0	1.81	0.90	4×550	4×600	32×100	239
2013 Mar 4.0	1.28	0.86	8×698	8×605	56×100	868

Extended Data Table 1 | Log of the VLT/X-shooter observations of SN 2010jl.

- [34] Benetti, S. *et al.* Supernova 2010jl in UGC 5189A. *Central Bureau Electronic Telegrams* **2536**, 1 (2010).
- [35] Stoll, R. *et al.* SN 2010jl in UGC 5189: Yet Another Luminous Type II_n Supernova in a Metal-poor Galaxy. *Astrophys. J.* **730**, 34 (2011). 1012.3461.
- [36] D’Odorico, S. *et al.* X-shooter UV- to K-band intermediate-resolution high-efficiency spectrograph for the VLT: status report at the final design review. In *Society of Photo-Optical Instrumentation Engineers (SPIE) Conference Series*, vol. 6269 of *Society of Photo-Optical Instrumentation Engineers (SPIE) Conference Series* (2006).
- [37] Vernet, J. *et al.* X-shooter, the new wide band intermediate resolution spectrograph at the ESO Very Large Telescope. *Astron. Astrophys.* **536**, A105 (2011). 1110.1944.
- [38] Modigliani, A. *et al.* The X-shooter pipeline. In *Society of Photo-Optical Instrumentation Engineers (SPIE) Conference Series*, vol. 7737 of *Society of Photo-Optical Instrumentation Engineers (SPIE) Conference Series* (2010).
- [39] Horne, K. An optimal extraction algorithm for CCD spectroscopy. *Publ. Astron. Soc. Pac.* **98**, 609–617 (1986).
- [40] Schlegel, D. J., Finkbeiner, D. P. & Davis, M. Maps of Dust Infrared Emission for Use in Estimation of Reddening and Cosmic Microwave Background Radiation Foregrounds. *Astrophys. J.* **500**, 525 (1998). astro-ph/9710327.

- [41] Rouleau, F. & Martin, P. G. Shape and clustering effects on the optical properties of amorphous carbon. *Astrophys. J.* **377**, 526–540 (1991).
- [42] Li, A. & Draine, B. T. Infrared Emission from Interstellar Dust. II. The Diffuse Interstellar Medium. *Astrophys. J.* **554**, 778–802 (2001). [astro-ph/0011319](#).
- [43] Fransson, C. *et al.* High Density Circumstellar Interaction in the Luminous Type II_n SN 2010jl: The first 1100 days. *ArXiv e-prints* (2013). [1312.6617](#).
- [44] Rauscher, T., Heger, A., Hoffman, R. D. & Woosley, S. E. Nucleosynthesis in Massive Stars with Improved Nuclear and Stellar Physics. *Astrophys. J.* **576**, 323–348 (2002). [astro-ph/0112478](#).
- [45] Dwek, E. The infrared echo of a type II supernova with a circumstellar dust shell - Applications to SN 1979c and SN 1980k. *Astrophys. J.* **274**, 175–183 (1983).
- [46] Soderberg, A. M. *et al.* An extremely luminous X-ray outburst at the birth of a supernova. *Nature* **453**, 469–474 (2008). [0802.1712](#).
- [47] Malesani, D. *et al.* Early Spectroscopic Identification of SN 2008D. *Astrophys. J. Lett.* **692**, L84–L87 (2009). [0805.1188](#).
- [48] Blinnikov, S., Lundqvist, P., Bartunov, O., Nomoto, K. & Iwamoto, K. Radiation Hydrodynamics of SN 1987A. I. Global Analysis of the Light Curve for the First 4 Months. *Astrophys. J.* **532**, 1132–1149 (2000). [astro-ph/9911205](#).

- [49] Tolstov, A. G., Blinnikov, S. I. & Nadyozhin, D. K. Coupling of matter and radiation at supernova shock breakout. *Mon. Not. R. Astron. Soc.* **429**, 3181–3199 (2013). 1212.3662.
- [50] Dwek, E. & Arendt, R. G. Infrared Echoes Reveal the Shock Breakout of the Cas A Supernova. *Astrophys. J.* **685**, 976–987 (2008). 0802.0221.

Supplementary Information

1 Origin of the lines and line attenuation

The different velocity components can be associated with different regions from which the emission arises. The intermediate velocity component ($\sim 400\text{--}4,000 \text{ km s}^{-1}$) in Type II_n supernovae is usually attributed to emission from a postshock region behind the forward shock, which penetrates the dense circumstellar medium (13, 18). The conspicuous narrow P Cygni lines arise from interaction with a slow unshocked circumstellar stellar wind (51). The presence of rather strong intermediate and narrow width hydrogen lines suggests that SN 2010jl has a hydrogen rich circumstellar medium, but has not shed all the hydrogen during its progenitor phase, which can be deduced from the broad component of H α (Extended Data Figures 3b and 5a).

Our high-resolution data set clearly shows that the intermediate- width emission lines (H, He) feature a progressive attenuation of their red wings. The attenuation effect is strongest for lines at the shortest wavelengths and gradually weakens towards lines at longer wavelengths (Figure 1). Furthermore, the red wing attenuation is accompanied by a corresponding wavelength dependent blueshift of the centroids of the lines (Extended Data Figure 6). These effects together with the temporally increasing attenuation and blueshifts point to ongoing dust formation in a shell like geometry, i.e., in a cool dense shell (CDS) behind the forward shock at the early epochs. The persistent blueshift and strong attenuation of the emission lines at the late epoch hint at dust formation in the ejecta (as the blueshift is detected in the ejecta metal lines).

Dust formation in the ejecta can be ruled out for the early epochs (26–239 days) because the

ejecta are still too hot to allow for dust condensation. Furthermore, emission lines of nucleosynthesized elements residing in the ejecta, which would show effects of dust formation in their profiles, are not detected. Thus, the majority of the ejecta material out of which dust can condense is still behind the optically thick and hot ($T_{\text{SN}} \approx 7,300 \text{ K}$) photosphere of the supernova (SN).

It is unlikely that the observed progressive attenuation and blueshift of the lines is due to occultation. The opaque ejecta could in principle block the light from the far side of the ejecta, leading to an attenuation of red light (emitted by receding material). However, the area of the photosphere ($R_{\text{SN}} \sim 2.5\text{--}3 \times 10^{15} \text{ cm}$) is just about 2 percent of that of the CDS ($R_{\text{CDS}} \sim 2 \times 10^{16} \text{ cm}$, see Methods and Supplementary Information section 2) from which we assume that the intermediate emission lines originate, making this effect negligible. Additionally, a pure occulting effect would lead to a decreasing attenuation of the emission lines with time because of the receding photosphere, which is the opposite of what we observe.

Alternatively, the photosphere is in front of the forward shock and the emission line velocities do not represent physical motion of the shock but are rather caused by Thomson electron scattering (13, 40, 52). As the photosphere recedes it will be located behind the forward shock and the CDS. At this point, the intermediate-width emission lines become less dominated by the Thomson electron scattering effect and their velocity widths correspond to the physical motion of either the forward shock or the CDS. The suggestion that the blueshifts and attenuations are obtained through electron scattering and occultation (14, 40) is however difficult to maintain. First, a significant effect due to electron scattering and occultation would require the lines to be formed at the photosphere (53) which is ruled out by polarimetric measurements (54) showing significant

depolarization of the intermediate width lines. Second, the wavelength dependent effect which we observe (Figure 1, Extended Data Figure 6), in particular the fact that the $n = 5$ transitions $H\gamma$ and $P\beta$ show different blueshifts, is difficult to attribute to electron scattering. Moreover, in this picture, the emission lines are expected to be symmetric, resembling Lorentzians. Although the hydrogen lines used in our studies are well approximated by Lorentzian profiles, they are not symmetric as illustrated in Extended Data Figure 5b. Some hydrogen emission lines have been excluded from our studies due to significant asymmetries and deviations from Lorentzian profiles (Methods). The emission lines at the late epoch (868 days) can no longer be approximated by Lorentzian profiles. Additionally, we detect significant broad components (Extended Data Figures 3, 4 and 5a, see also Ref. 54) which would not be visible if the shell is optically thick. These broad lines suggest large velocities which would quickly overtake the CDS (Extended Data Figure 4). Furthermore, we infer a black body radius, R_{SN} , which is temporally receding (Methods). We attribute this to the receding photosphere rather than an optically thick shell at the shock interaction region. Such an optically thick shell would be expected to either remain at constant radius or increase with time due to the expanding forward shock.

Finally, the suggestion (12) that there is a large difference in the blueshifts between the blue ($H\gamma$) and red ($B\gamma$) is not supported by our observations. We attribute this conclusion to the low signal to noise ratio and the low resolution of the spectra upon which that conclusion was reached.

2 Constraining the locations and sources of dust formation

To determine the location of the CDS we require $R_{\text{vap}} \lesssim R_{\text{CDS}} \lesssim R_{\text{shock}}$ and consistency between the extinction and emission dust masses. At 26 days, the blast wave reaches a radius $R_{\text{shock}} \gtrsim 2 \times 10^{16}$ cm for an assumed fast initial blast wave velocity of 3.5×10^4 km s⁻¹. As the SN blast wave decelerates to a velocity of about $\sim 3,000$ km s⁻¹, a CDS forms at a location $R_{\text{CDS}} \lesssim R_{\text{shock}}$ (both of these radii increase with time). Any dust must be located beyond the vaporization radius, R_{vap} , of the nearly constant observed SN radiation. From Extended Data Figure 8 we find that (at 26 days) $R_{\text{vap}} \lesssim 2 \times 10^{16}$ cm for carbonaceous dust with grain radii $\gtrsim 0.25$ μm and temperature $T_{\text{dust}} \lesssim T_{\text{hot}}$ while grains $\lesssim 0.25$ μm have higher temperatures of 2,200–2,700 K. The calculated temperatures of the large dust grains at that location is consistent with those inferred from the modified black-body fits to the NIR emission.

Extended Data Figure 9b shows that the derived radius-dependent extinction dust mass, the dust mass from the NIR emission, and the characteristic radii of the system, R_{vap} and R_{shock} , lead to a joint constraint on the location of the dust formation site of $R_{\text{CDS}} \approx 2.0 \times 10^{16}$ cm. An alternative location for early dust formation between 26–239 days, such as the SN ejecta, does not meet the above requirements and is therefore disfavoured.

It has been pointed out (14) that there is very little colour evolution, implying little extinction along the line of sight to the photosphere. This suggests that the dust formed outside the line of sight, e.g., in a non-spherical geometry or in an inhomogeneous CDS. The light from the region emitting the intermediate velocity component emission lines traverses the dust forming CDS,

which does give rise to the extinction of the lines. Alternatively, a clumpy medium can give rise to a flat extinction curve (55, 56). In our case, however, the constancy of the extinction curve with time rules out that clumpiness is the cause of the flatness unless the increase in extinction is balanced by a corresponding change in the covering fraction.

At the late epoch (868 days) the inferred carbon dust mass from the NIR emission is more than 10 times larger than the dust mass at 239 days (Figure 4). The temperature of the dust has dropped to about 1,100 K and a larger black-body radius of $\approx 5.7 \pm 0.2 \times 10^{16}$ cm is inferred from fits to the NIR emission (Extended Data Figure 2). The CDS, which has a typical velocity of $\lesssim 3,000 \text{ km s}^{-1}$, as inferred from the intermediate velocity component emission lines (Methods, Supplementary Information sections 1 and 4), will not have reached such a large radius. Moreover, the bulk ejecta material traveling with an average expansion velocity $v_{ej} \approx 7,500 \text{ km s}^{-1}$, as measured during the first 236 days (Extended Data Figure 4), will have caught up with the CDS already. This disfavours continued dust formation at an accelerated rate in the CDS. Instead, an additional dust source must emerge between 239 days and 868 days.

We favour dust formation in an interaction region of the ejecta bulk material with swept up CSM. The bulk material of the ejecta will have reached a large radius corresponding to the derived black-body radius at 868 days ($(5.7 \pm 0.2) \times 10^{16}$ cm). This interpretation is supported by the highly attenuated and blueshifted hydrogen and oxygen emission lines (Figure 1). Such an effect can only occur when the dust formation region resides inside or at the line emitting region. Furthermore, the oxygen lines are likely ejecta lines and thus strongly suggest that ejecta material is involved in the dust formation at late times. The supply of large amounts of dust forming ejecta material can

explain the sudden acceleration in the build-up of the dust mass (Figure 4).

At late times the UBVRI optical lightcurves significantly drop (12, 24). The synthetic photometry of the late epoch (868 days) shows a continued drop in the optical bands while the H and K band lightcurves increase. This is reflected in the temporal evolution of the UV-optical (UVO) and NIR energy output shown in Extended Data Figure 7b. The drastic UVO drop has been attributed to dust formation (12), presumably at the onset of the accelerated dust formation detected here (Figure 4). On the other hand, we find that the evolution of the total bolometric luminosity continues to follow a $t^{-0.4}$ power-law, such as that found for the UVO lightcurve before the drop (24). While at early times, the NIR emission is caused by the newly formed dust in the CDS, the dramatic change in the evolution of the light curves after day ~ 236 , suggests a different origin for the NIR emission at late epochs ($\gtrsim 240$ days). This may be due to newly formed dust including ejecta material. At this stage, the UVO luminosity from the shock interaction must be very efficiently absorbed and reradiated by the forming dust, providing an important constraint on any dust formation or evolution mechanism.

We propose a two-stage dust-formation mechanism. In the first stage, only CSM material is responsible for the formation of dust and in the second stage CSM and ejecta bulk material are involved. This is consistent with the evolution of the total bolometric luminosity (Extended Data Figure 7) which follows a $t^{-0.4}$ power law behavior up to 868 days. However, this implies that the SN did not yet enter the snow-plow phase (conservation of momentum; the radiated energy behind the shock is comparable to the energy of the explosion) of its evolution on day 868, contrary to suggestions in the literature (24). Presumably, the UVO luminosity is powered by a central

light source, possibly by the interaction at the low radius of $R_{\text{SN}} \sim 2.4\text{--}3.2 \times 10^{15}$ cm between an aspherical, very high density SN progenitor outflow and the blastwave and ejecta material, which leads to optically thick emission. As mentioned above, the fact that the early dust formation in the CDS at R_{CDS} does not cause substantial extinction of the UVO light suggests that dust initially forms outside the line of sight. The drastic drop in the UVO lightcurve (Extended Data Figure 7) is then due to extinction of the UVO radiation directly in the line of sight by the efficiently forming dust with the aid of ejecta material at large radius ($(5.7 \pm 0.2) \times 10^{16}$ cm). The central light source will heat the dust at large radius to the observed temperature of $\sim 1,100$ K and cause the simultaneous rise in the NIR luminosity. We want to stress that the embedded heating sources from the radioactive decay of ^{56}Co and the isotope ^{44}Ti cannot power the observed NIR luminosities in SN 2010jl (Extended Data Figure 7). The geometry may be reminiscent of that of η Car, which shows several very dense circumstellar arcs out to a few times 10^{16} cm (57).

3 Ruling out pre-existing dust

The spectra exhibit narrow absorption lines from the resolved Na I doublet arising from absorption by material at the redshift of the SN as well as from the interstellar medium in the MW. We measure a total Na ID equivalent width (EW) of 0.354 ± 0.004 Å at the redshift of the SN. This translates into a host galaxy $E(B - V) = 0.037 \pm 0.007$ mag (58), i.e., $A_V = 0.11 \pm 0.02$ mag for $R_V = 3.1$. For the MW foreground we measure $\text{EW} = 0.166 \pm 0.004$ Å from the Na ID lines, which corresponds to $E(B - V) = 0.022 \pm 0.004$ mag, i.e., $A_V = 0.07 \pm 0.02$ mag. This is consistent with the value obtained from maps of dust IR emission (37) used to correct our spectra for foreground extinction

($E(B - V) = 0.027$ mag) and the most recent recalibration ($E(B - V) = 0.024$ mag) based on Sloan Digital Sky Survey stellar spectra (59). The combined host+MW $E(B - V)$ is 0.06 ± 0.01 mag. The Serkowski law (60), $P_{\max} = 9E(B - V) \%$, implies $P < 0.6 \%$, consistent with the measured $P < 0.3 \%$ for the SN intermediate line emission (54). The Na ID and polarization measurements set strong constraints on the reddening of the SN and hence on the total dust column along the line of sight.

The lack of foreground dust extinction must be reconciled with the very high metal column density inferred from X-ray absorption observations. SN 2010jl was observed with *Chandra* at two epochs, on 2010 Dec 7 UT and 2011 Oct 17 UT (31). At the first epoch a very large equivalent hydrogen column density of $1 \times 10^{24} \text{ cm}^{-2}$ was inferred from soft X-ray absorption. At the second epoch this had dropped to $3 \times 10^{23} \text{ cm}^{-2}$. Applying a standard MW conversion factor between A_V and N_H (61) and accounting for the assumed metallicity (31) this would correspond to A_V of 136 and 40 mag, respectively. Clearly SN 2010jl was not extinguished by this much dust, confirming that most of any pre-existing dust must have been vaporized by the SN out to radii larger than R_{cav} of about 10^{17-18} cm (Methods).

Furthermore, from Extended Data Figure 1 it is evident that while the *Spitzer*/IRAC $3.6 \mu\text{m}$ observations of SN 2010jl (11) are well-reproduced by our modified black-body fit to the X-shooter data, there is significant excess emission in the $4.5 \mu\text{m}$ band. This has been interpreted as being due to a cold component of pre-existing dust emitting at 750 K in a torus around the SN (11). However, the model upon which that claim was reached cannot account for the NIR excess in the range of $1-2.3 \mu\text{m}$, evident in all our spectra (Extended Data Figures 1 and 2). As demonstrated

in our analysis, a hot dust component of $\sim 1,800$ K is required to account for the NIR excess and simultaneously for the $3.6 \mu\text{m}$ emission. Additionally, as shown in Extended Data Figure 8, no dust with temperatures $\lesssim 1,500$ K can exist at the location of the CDS. Thus, any such cool dust must be placed outside the dust free cavity at radii $\gtrsim R_{\text{cav}}$, which we disfavoured based on the extinction constraints presented above.

Alternatively, the remaining excess $4.5 \mu\text{m}$ emission could be interpreted as due to $4.7 \mu\text{m}$ fundamental band emission of carbon monoxide (CO). Following the first detection of CO (fundamental band and first overtone at $2.3 \mu\text{m}$) in SN 1987A (62, 63, 64), CO has been detected in numerous Type II SNe, including the detection of the first overtone in the Type II_n SN 1998S (see Ref. 65, for an overview). Excess $4.5 \mu\text{m}$ band photometric excess has previously been attributed to the CO fundamental band in Type II SNe, e.g., in SN 2007it (66). CO is an abundant molecule which forms at very high temperatures (up to $\sim 5,000$ K), and acts as strong coolant through its rotational-vibrational transitions. Thus, it is considered to significantly influence subsequent dust formation (65, 67, 68). The possible detection of CO adds to the evidence that conditions are right for the early formation of dust in SN 2010jl.

The hot NIR emission of the early epochs cannot be attributed to a thermal echo generated by pre-existing dust heated by a short burst of far UV radiation associated with the shock breakout. Such a burst will have vaporized any pre-existing dust in the CSM out to about 10^{17-18} cm (Extended Data Figure 8), much larger than the NIR black-body radius. The surviving dust will reradiate the absorbed energy from the burst, giving rise to a NIR echo with temperatures between 1,500 to 2,000 K, depending on dust grain radii and composition. The locus of the emitting dust

describes an ellipsoid of revolution with a thickness $\lesssim 1$ light day, with one focus centred on the SN and the other on the observer. At time t , the radiating dust lies on the intersection of the ellipsoid with the (assumed) sphere of surviving dust, creating an annulus with a projected area $A \approx 2\pi c^2 t \Delta t$. The total mass of radiating dust constitutes a fraction equal to $A/4\pi(ct)^2 = \Delta t/2t$ of the surviving circumstellar dust. On day 66 past peak (assuming this is about $t \approx 100$ d past explosion) the mass of hot dust observed in the SN spectrum is about $M_{\text{hot}} \approx 5 \times 10^{-5} M_{\odot}$. If attributed to an echo, the total mass of dust in the shell must be $2t/\Delta t \approx 200$ times larger. The visual optical depth of such shell is then $\tau_V = \tau(\lambda = 0.55\mu\text{m}) \approx 200 \times (M_{\text{hot}}/4\pi R_{\text{cav}}^2) \kappa_V$. For $\kappa_V \approx 3 \times 10^4 \text{ cm}^2 \text{ g}^{-1}$, the visual optical depth $\tau_V \approx 0.5$. This value is significantly larger than the observed upper limit of $\tau_V \lesssim 0.1$. Thus, the large mass of surviving dust needed to give rise to an echo will violate the observed upper limits on the amount of intervening extinction, ruling out a NIR echo (40) as the source of the early hot NIR emission. At early epochs, the dust emission therefore most likely originates from inside the vaporization zone, where the subsequently forming dust gives rise to both the extinction and the NIR emission. This supports the constraints on the dust formation location derived in Supplementary Information section 4.

The NIR emission at late times (> 300 days) has been attributed to a dust echo from pre-existing dust (40). We find that at late epochs, the observed NIR emission cannot be attributed to an echo from pre-existing dust, which escaped vaporization by the shock breakout. In this picture, the break in the UVO luminosity is not caused by extinction. This would suggest that the SN shock has entered the snowplow phase of its evolution after day ~ 300 , or propagated beyond the outer boundary of the CSM. The SN light curve can then be thought of as a top-hat function with an

average luminosity of $\sim 3 \times 10^9 L_{\odot}$ and a width of ~ 250 days. Furthermore, the dust could not be distributed in a shell, since we would then expect a NIR echo of the same intensity as the flux on days 553 (12) and 868 at earlier epochs as well, which is contrary to our observations. The dust must therefore be distributed in a torus with an inner radius of 275 light days, to give rise to the observed flux on day 553. The cross-sectional radius of the torus may be much smaller than the width of the SN lightcurve (~ 250 light days), in which case the echo on day 553 is caused by the encounter of the ring with the leading edge of the SN lightcurve, and that on day 868 by its trailing edge. The dust temperature is expected to be only about 600 K, since the UVO flux incident on the dust is smaller by a factor of $\sim 10^3$ than that incident on the dust heated by the shock breakout ($L \approx 10^{11} L_{\odot}$, Methods) to $\sim 2,500$ K at a distance of 40 light days (Extended Data Figure 8). An echo origin for the NIR emission observed on days 553 and 868 can therefore be definitely ruled out. Finally, the NIR luminosity on day 868 is about one third of the average UVO luminosity during the ~ 30 – 300 day interval (Extended Data Figure 7), an excessively high fraction of the UVO luminosity to be intercepted by a dust torus.

4 Properties of the early dust formation site

The rapid formation of large dust grains requires a gas density of order $\sim 10^{9-11} \text{ cm}^{-3}$ and temperatures below $\sim 3,000$ K. The CDS is therefore considered as the likely dust formation site (see Ref. 33, for a simulation of a forming CDS). We can estimate the density of the dust-forming region from the X-ray observations that were conducted at 50 and 364 days past peak (31, 32). The observations suggest a gas temperature of about 8–10 keV ($\sim 10^8$ K). For a strong shock, the

postshock gas temperature $T_{\text{gas}}(K) = (3/16) k^{-1} \mu v_s^2$, where v_s^2 is the velocity of the forward shock propagating through the dense shell, k is the Boltzmann constant and μ is the molecular weight of a fully ionized gas (see Ref. 69). For a T_{gas} corresponding to the (X-ray) gas temperature, we infer a shock velocity of $\sim 3,000 \text{ km s}^{-1}$, as also found in Ref (24). The first evidence for dust formation was present in the spectra obtained 44 days past peak. We assume that the shock had collided with the dense shell shortly before our first observation, which requires that the gas had to cool within less than ~ 18 days from $\sim 10^8$ to $3,000 \text{ K}$.

The cooling time of a hot plasma is given by

$$\tau_{\text{cool}} = \frac{kT_{\text{gas}}}{n_e \Lambda(T_{\text{gas}})}, \quad (5)$$

where n_e is the electron density of the postshock gas and $\Lambda(T_{\text{gas}})$ is the cooling function. For X-ray emitting plasmas, $\Lambda(T_{\text{gas}}) \approx 2 \times 10^{-23} \text{ erg s}^{-1} \text{ cm}^3$ at temperatures of $\approx 3 \times 10^7 \text{ K}$, the ‘bottle neck’ temperature where cooling is least efficient (69, 70). We estimate the density of the postshock gas from the observed change in the hydrogen column density of the preshock shell between the two X-ray observations, $\Delta N_{\text{H}} = 7 \times 10^{23} \text{ cm}^{-2}$, which is attributed to the passage of the forward shock through the shell. The average density of the preshock shell is then given by $n_{\text{H}} = \Delta N_{\text{H}} / (v_s \Delta t) \approx 10^8 \text{ cm}^{-3}$, taking $\Delta t = 314 \text{ d}$ as the time interval between the two X-ray observations. For a strong shock the corresponding postshock density is $4 n_{\text{H}}$, which results in a cooling time of $\tau_{\text{cool}} \approx 6$ days according to equation (1). Once the gas has cooled below $\sim 3 \times 10^7 \text{ K}$, rapid cooling via atomic line transitions will further compress and cool the gas (69). Using the approximation of an ‘isothermal shock’ we find that the density reached in the CDS will be $\gtrsim 10^{10} \text{ cm}^{-3}$ for the required temperature of the CDS. Similarly, if we assume that all the swept up material will be

compressed into the CDS, we derive a density of the CDS from the X-ray observations as $n_{\text{H,CDS}} = \Delta N_{\text{H}} / \Delta R_{\text{CDS}} \sim 5 \times 10^{9-10} \text{ cm}^{-3}$ for an adopted thickness of the CDS $\Delta R_{\text{CDS}} = 1\text{--}10 \text{ AU}$ (33). We can approximate the minimum mass of the CDS from the swept up material between the two X-ray observations as $M \approx 4\pi m_{\text{H}} R_{\text{CDS}}^2 n_{\text{H}} v_{\text{s}} \Delta t = 4\pi m_{\text{H}} R_{\text{CDS}}^2 \Delta N_{\text{H}} \approx 3 M_{\odot}$, where $R_{\text{CDS}} = 2 \times 10^{16} \text{ cm}$ is the assumed location of the CDS (Extended Data Figure 9b). The corresponding amount of metals is $\approx 0.02 M_{\odot}$. Furthermore, we estimate an accretion timescale (71) for dust grains with grain radii $a \lesssim 0.5 \mu\text{m}$ in such a CDS of $\lesssim 40$ days, which is about the time between the first and third observation. However, to grow grains $> 0.5 \mu\text{m}$ within the same time through accretion higher densities are required. Alternatively, dust grains grow through coagulation rather than accretion.

The above estimates of the cooling time of the postshock gas, the density of the CDS and mass of metals in the CDS are in good agreement with the requirements for rapid formation of dust. Comparison of the derived mass of metals to the inferred extinction and emission dust masses suggests a condensation efficiency of $\approx 1 \%$ in the CDS.

5 Attaining large grain sizes and dust masses

Our estimated carbon dust mass of $\approx 2 \times 10^{-3} M_{\odot}$ at the late epoch (868 days) most likely represents a lower limit. The inferred dust temperature from fits to the NIR emission allows for dust grain species other than carbon to be formed. Therefore, we explored different dust models (Methods) and found that either amorphous carbon or silicates can adequately fit the NIR emission. However, in either case, large grains provide good fits, while small carbon grains cannot be dominant. For any model, the temperature range of the dust causing the NIR emission is between $\sim 1,000\text{--}1,300$

K and the inferred amount of dust is for amorphous carbon $\sim 0.001\text{--}0.005 M_{\odot}$ and $\sim 0.006\text{--}0.023 M_{\odot}$ for silicate dust.

There is copious evidence of dust formation in the ejecta of Type IIP SNe (1, and references therein). The theoretical models available in the literature are primarily designed to model dust formation in the ejecta of SNe without a dense CSM, such as e.g., Type IIP or pair instability SNe (25, 67, 68, 72, 73, 74), or Type Ib and IIb SNe (75, 76). In these models, the density and temperature of the dust formation site (the ejecta) rapidly decline. Consequently, the time available for dust nucleation, which only happens in a certain range of high densities and moderate temperatures (77, 78), is short. Subsequent grain growth at lower temperatures and densities becomes rapidly inefficient due to the fast declining densities. So far, dust nucleation and growth can be accommodated up to 5 years after explosion (25), although grains grow to sizes no larger than ($0.1\text{--}0.2 \mu\text{m}$) (25, 68). There are no dust formation models for luminous Type IIn SNe with a dense CSM, such as SN 2010jl (24). The SN ejecta, which sweeps up the dense CSM, could sustain higher densities over a longer period of time than predicted in the models without a CSM, leading to efficient grain growth and larger grains as found in this paper.

Alternatively, for ejecta dust formation, higher dust masses are inferred when invoking a clumpy structure of the dust forming region (17, 79, 80). Unfortunately the dust mass sensitively depends on the unknown optical depth of the clumps as well as the clump filling factors and distribution, making dust mass estimates uncertain. Nevertheless, a clumpy structure is possible at the late epoch, even though it has been ruled out for the early dust formation in the CDS (Supplementary Information section 2). There are no theoretical models addressing dust formation and growth

in SNe featuring CSM – ejecta interaction. More sophisticated radiative transfer modeling would be important to gain further insight into dust mass and grain size estimates.

- [51] Smith, N. *et al.* A Massive Progenitor of the Luminous Type II_n Supernova 2010jl. *Astrophys. J.* **732**, 63 (2011). 1011.4150.
- [52] Chugai, N. N. Broad emission lines from the opaque electron-scattering environment of SN 1998S. *Mon. Not. R. Astron. Soc.* **326**, 1448–1454 (2001). astro-ph/0106234.
- [53] Dessart, L., Hillier, D. J., Gezari, S., Basa, S. & Matheson, T. SN 1994W: an interacting supernova or two interacting shells? *Mon. Not. R. Astron. Soc.* **394**, 21–37 (2009). 0804.0428.
- [54] Patat, F., Taubenberger, S., Benetti, S., Pastorello, A. & Harutyunyan, A. Asymmetries in the type II_n SN 2010jl. *Astron. Astrophys.* **527**, L6 (2011). 1011.5926.
- [55] Berlind, A. A., Quillen, A. C., Pogge, R. W. & Sellgren, K. The Extinction Law in an Occulting Galaxy. *Astron. J.* **114**, 107–114 (1997). astro-ph/9704156.
- [56] Szomoru, A. & Guhathakurta, P. Extinction Curves, Distances, and Clumpiness of Diffuse Interstellar Dust Clouds. *Astron. J.* **117**, 2226–2243 (1999). astro-ph/9901422.
- [57] Teodoro, M., Madura, T. I., Gull, T. R., Corcoran, M. F. & Hamaguchi, K. Detection of the Compressed Primary Stellar Wind in η Carinae. *Astrophys. J. Lett.* **773**, L16 (2013). 1307.3244.
- [58] Poznanski, D., Prochaska, J. X. & Bloom, J. S. An empirical relation between sodium absorption and dust extinction. *Mon. Not. R. Astron. Soc.* **426**, 1465–1474 (2012). 1206.6107.

- [59] Schlafly, E. F. & Finkbeiner, D. P. Measuring Reddening with Sloan Digital Sky Survey Stellar Spectra and Recalibrating SFD. *Astrophys. J.* **737**, 103 (2011). 1012.4804.
- [60] Serkowski, K., Mathewson, D. S. & Ford, V. L. Wavelength dependence of interstellar polarization and ratio of total to selective extinction. *Astrophys. J.* **196**, 261–290 (1975).
- [61] Watson, D. The Galactic dust-to-metals ratio and metallicity using gamma-ray bursts. *Astron. Astrophys.* **533**, A16 (2011). 1107.6031.
- [62] Spyromilio, J., Meikle, W. P. S., Learner, R. C. M. & Allen, D. A. Carbon monoxide in supernova 1987A. *Nature* **334**, 327–329 (1988).
- [63] Catchpole, R. M. *et al.* Spectroscopic and photometric observations of SN 1987A. III - Days 135 to 260. *Mon. Not. R. Astron. Soc.* **231**, 75P (1988).
- [64] Danziger, I. J., Bouchet, P., Fosbury, R. A. E., Gouiffes, C. & Lucy, L. B. SN 1987A - Observational results obtained at ESO. In Kafatos, M. & Michalitsianos, A. G. (eds.) *Supernova 1987A in the Large Magellanic Cloud*, 37–50 (1988).
- [65] Cherchneff, I. & Sarangi, A. Molecules in Supernova Ejecta. In Cernicharo, J. & Bachiller, R. (eds.) *IAU Symposium*, vol. 280 of *IAU Symposium*, 228–236 (2011). 1107.5668.
- [66] Andrews, J. E. *et al.* Photometric and Spectroscopic Evolution of the IIP SN 2007it to Day 944. *Astrophys. J.* **731**, 47 (2011). 1102.2431.
- [67] Todini, P. & Ferrara, A. Dust formation in primordial Type II supernovae. *Mon. Not. R. Astron. Soc.* **325**, 726–736 (2001). astro-ph/0009176.

- [68] Nozawa, T., Kozasa, T., Umeda, H., Maeda, K. & Nomoto, K. Dust in the Early Universe: Dust Formation in the Ejecta of Population III Supernovae. *Astrophys. J.* **598**, 785–803 (2003). [astro-ph/0307108](#).
- [69] Draine, B. T. *Physics of the Interstellar and Intergalactic Medium* (2011).
- [70] Dere, K. P. *et al.* CHIANTI - an atomic database for emission lines. IX. Ionization rates, recombination rates, ionization equilibria for the elements hydrogen through zinc and updated atomic data. *Astron. Astrophys.* **498**, 915–929 (2009).
- [71] Dwek, E. & Cherchneff, I. The Origin of Dust in the Early Universe: Probing the Star Formation History of Galaxies by Their Dust Content. *Astrophys. J.* **727**, 63 (2011). [1011.1303](#).
- [72] Nozawa, T. *et al.* Evolution of Dust in Primordial Supernova Remnants: Can Dust Grains Formed in the Ejecta Survive and Be Injected into the Early Interstellar Medium? *Astrophys. J.* **666**, 955–966 (2007). [0706.0383](#).
- [73] Bianchi, S. & Schneider, R. Dust formation and survival in supernova ejecta. *Mon. Not. R. Astron. Soc.* **378**, 973–982 (2007). [0704.0586](#).
- [74] Cherchneff, I. & Dwek, E. The Chemistry of Population III Supernova Ejecta. II. The Nucleation of Molecular Clusters as a Diagnostic for Dust in the Early Universe. *Astrophys. J.* **713**, 1–24 (2010). [1002.3060](#).
- [75] Nozawa, T. *et al.* Early Formation of Dust in the Ejecta of Type Ib SN 2006jc and Temperature and Mass of the Dust. *Astrophys. J.* **684**, 1343–1350 (2008). [0801.2015](#).

- [76] Nozawa, T. *et al.* Formation and Evolution of Dust in Type IIb Supernovae with Application to the Cassiopeia A Supernova Remnant. *Astrophys. J.* **713**, 356–373 (2010). [0909.4145](#).
- [77] Feder, J., Russell, K. C., Lothe, J. & Pound, G. M. Homogeneous nucleation and growth of droplets in vapours. *Advances in Physics* **15**, 111–178 (1966).
- [78] Sedlmayr, E. From Molecules to Grains. In Jorgensen, U. G. (ed.) *IAU Colloq. 146: Molecules in the Stellar Environment*, vol. 428 of *Lecture Notes in Physics*, Berlin Springer Verlag, 163 (1994).
- [79] Sugerman, B. E. K. *et al.* Massive-Star Supernovae as Major Dust Factories. *Science* **313**, 196–200 (2006). [astro-ph/0606132](#).
- [80] Ercolano, B., Barlow, M. J. & Sugerman, B. E. K. Dust yields in clumpy supernova shells: SN 1987A revisited. *Mon. Not. R. Astron. Soc.* **375**, 753–763 (2007). [astro-ph/0611719](#).